Check for updates

Recent developments in the construction and applications of platinum-based metallacycles and metallacages *via* coordination†

Yan Sun, [ID] *[ad] Chongyi Chen, [ID] [b] Jianbo Liu[c] and Peter J. Stang[d]

Coordination-driven suprastructures have attracted much interest due to their unique properties. Among these structures, platinum-based architectures have been broadly studied due to their facile preparation. The resultant two- or three-dimensional (2D or 3D) systems have many advantages over their precursors, such as improved emission tuning, sensitivity as sensors, and capture and release of guests, and they have been applied in biomedical diagnosis as well as in catalysis. Herein, we review the recent results related to platinum-based coordination-driven self-assembly (CDSA), and the text is organized to emphasizes both the synthesis of new metallacycles and metallacages and their various applications.

1. Introduction

Supramolecular interactions are key to the high complexity and functionality of intricate and functional molecular assemblies, and they have led to the emergence of novel materials.[1–3] The self-organization of simple molecular building blocks into functional materials is a common strategy in the development of such suprastructures.[4–6] Among various strategies for

self-assembly, coordination-driven self-assembly (CDSA) is one of the most powerful and influential strategies.[7–17] By choosing appropriate metal ions and *via* the sensible design of the building blocks, metal–organic complexes (MOCs) with various sizes, shapes and metal (M)/ligand (L) ratios have been obtained through CDSA.[18–20]

The first coordination macrocycle was made by Verkade,[21] and several methodologies for the design and preparation of MOCs have been reported since then.[22,23] The directional bonding method,[24] the molecular panelling approach,[25] the symmetry interaction strategy,[12] and the weak link strategy[26] were introduced and developed by Fujita,[8] Stang,[9–11] Raymond,[12] Mirkin,[13] Newkome,[14] and Nitschke.[15–17] To date, crucial design principles have been established. The dynamic noncovalent interactions between metal centres and ligands as well as their shapes play essential roles in the controllable synthesis of target suprastructures.[7–17]

[a] *School of Chemistry and Chemical Engineering, Yangzhou University, Yangzhou, Jiangsu, 225002, P. R. China. E-mail: sunyan@yzu.edu.cn*

[b] *Ningbo Key Laboratory of Specialty Polymers, School of Materials Science and Chemical Engineering, Ningbo University, Ningbo, Zhejiang 315211, P. R. China*

[c] *Department of Radiology and Biomedical Imaging, University of California San Francisco, San Francisco, California 94107, USA*

[d] *Department of Chemistry, University of Utah, 315 South 1400 East, Room 2020, Salt Lake City, Utah 84112, USA*

† Dedicated to Eric V. Anslyn.

Yan Sun obtained her PhD degree at the Institute of Chemistry, Chinese Academy of Sciences, in 2012. Her research interests mainly focus on the synthesis and application of novel functional materials, multi-level and higher-ordered assembly. She joined Peter J. Stang's group at University of Utah in 2017, and now she is investigating metal–organic complexes (MOCs) and MOC-based multi-level assembly.
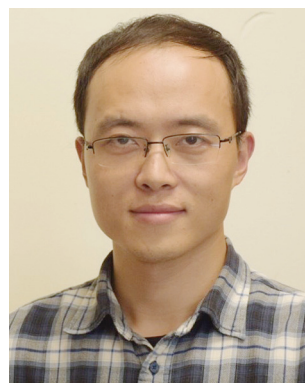
Yan Sun

Chongyi Chen obtained his BS degree in Chemistry in 2008 from the University of Science and Technology of China, his PhD degree in 2013 from Peking University and Institute of Chemistry, Chinese Academy of Sciences. He is currently an Associate Professor in the Department of Polymers at Ningbo University. His research interests include polypeptide-based chemistry and materials.

Chongyi Chen

This journal is © The Royal Society of Chemistry 2020

Chem. Soc. Rev., 2020, **49**, 3889–3919 | **3889**

To date, a wide range of metallacycles and metallacages with various geometries and sizes have been reported.[8–11] With such a diverse array of structures accessible, efforts have shifted from simply making new architectures to generating functional systems and exploiting their properties.[17,27,28] MOCs with interesting biological[29,30] and photophysical properties[31–33] have been developed. This review will focus on the recent advances in this field and our contributions of discrete multicomponent assembled systems based on platinum(II) metallacycles and metallacages. Both the construction of new structures and their properties are described in this review.

2. Design and synthesis

Recently, a wide variety of 2D systems (such as rhomboids,[34–41] squares,[42,43] rectangles,[44,45] triangles,[46] and double rhomboids[47]) and 3D systems (trigonal prisms,[48–51] tetragonal prisms,[52] cubes,[53–57] hexagonal prisms,[58,59] adamantanoids,[60,61] and a variety of other cages) have been prepared. In this section, the synthetic and structural features of the assembled metallacycles and metallacages will be emphasized. Their functional properties will be discussed in a separate subsection.

2.1 Metallacycles

As reported before, molecular rhomboids can be prepared by the combination of 60° acceptor units and 120° donors (Table 1). For example, combinations of a 60° functional Pt(II) acceptor (**Pt1**) with 120° donor ligand modified with triphenylamine (TPA) derivatives with various alkyl chains (**N1–3**) resulted in the formation of a series of di-TPA rhomboidal metallacycles (**M1–3**)[36] in excellent yields (Table 1). **M4–5**,[47] possessing hydrophobic or hydrophilic dendrons, were prepared through the assembly of dipyridyl ligands **N4** and **N5** with **Pt1**.[47] **M6**,[62] containing two alkynyl platinum(II) bzimpy moieties, was prepared by mixing ligand **N6** with **Pt1** in a mixed solvent of acetone/water.[62] Similarly, using a bis(pyridyl) subunit possessing a tethered C_{60} molecule (**N7**) with **Pt1** gave a rhomboid (**M7**)[63] with C_{60} units.

Pyrene-functionalized 120° donor ligands **N8** and **Pt1** were used to prepare rhomboid **M8**.[35]

The self-sorting of **N9**, with dipyridyl ligands of distinct sizes, with **N4**, **N5** and complementary organoplatinum(II) **Pt1** lead to the formation of **M9**[47] (1:1:1:4 ratio).[47] To study the effects of the counteranions on the functional properties, **Pt2**, possessing OTf^- instead of ONO_2^-, was prepared.

For example, the [2 + 2] assembly of 60° diplatinum acceptor **Pt2** and 120° donor **N11** gave rhomboid **M11** (Table 2).[64] Similarly, **Pt1/2** and 120° TPE-based dipyridyl ligand **N10** and pyrene functionalized ligand **N12** were combined to furnish rhomboids **M10/12**.[35,65] To provide hydrogen bonding sites to drive further assembly, 2-ureido-4-pyrimidinone (UPy)-functionalized 120° **N13** was used to construct **M13**.[34] For biomedical applications, rhomboidal metallacycle **M14**[38] was prepared by heating 120° dipyridyl donors **N14** and **Pt2** at 50 °C in methanol for 24 h. Recently, the modification of suprastructures *via* host–guest interactions has become an efficient and facile strategy for tuning the functions of the materials. Using this method, phenanthrene-21-crown-7 (P21C7)-containing acceptor **Pt3** was prepared (Table 3). At room temperature, **M15–17**[41] were prepared by mixing **Pt3** with 120° dipyridyl donors **N11**, **N15**, or **N16**, respectively, in dichloromethane for 24 h.[41] To prepare metallacycle-based fluorescent supramolecular polymers with designed properties, our group described the synthesis of metallacycles **M18–25**,[37] which are composed of **Pt3** and 120° dipyridyl donors **N17–24**.[37] Subsequently, ligands possessing a terpyridyl moiety and other substituents were prepared, and **Pt3** could assemble with 120° dipyridyl moieties (**N25–28**) to produce rhomboids **M26–29**[66] to form heterometallic supramolecular polymers through CDSA and host–guest interactions.[66]

As shown in Table 4, to obtain larger rhomboids, 60° diplatinum acceptor **Pt4** was prepared. The [2 + 2] assembly of 120° donor **N10** with **Pt4** gave **M30**.[64] **M31**[67] was prepared by assembling 120° ligand **N29** with **Pt4** in a 1:1 molar ratio.[67] **M32**[59] was then prepared in one pot *via* two-component CDSA by mixing ligand **O1** with **Pt4** in a 1:1 ratio first in a solution of H_2O/CD_2Cl_2 and then in CD_2Cl_2.[59] The self-assembly of **O2** with **Pt4** yielded triangular **M33**.[68] To investigate the biomedical applications of these structures, a platinum acceptor modified

Jianbo Liu obtained his PhD degree at the Shanghai institutes of Organic Chemistry, Chinese Academy of Science (SIOC) in 2016. He worked as a postdoctoral fellowship at University of Utah in 2017–2019. Then he continued his postdoc research in the University of California, San Francisco. His research interest is organic fluorine chemistry and asymmetric catalysis.

Jianbo Liu

Peter J. Stang is the David P. Gardner distinguished professor of Chemistry. He is a member of the US National Academy of Sciences, a foreign member of the Chinese Academy of Sciences, and the recipient of the Chinese Government "International Cooperation Award in Science and Technology" (2016), the ACS Priestley Medal (2013), and the US National Medal of Science (2011).

Peter J. Stang

Table 1 **Pt1** (anion:ONO_2^-)-based rhomboids (**M1–9**)

Acceptor	Donor	Ratio	Structure
	N1-3 R = H, OC_4H_9, OC_8H_{17}	2 + 2	**Metallacycle M1-3**
Pt 1	**N4**	2 + 2	**Metallacycle M4**
	N5	2 + 2	**Metallacycle M5**
	N6	2 + 2	**Metallacycle M6**
	N7	2 + 2	**Metallacycle M7**
	N8	2 + 2	**Metallacycle M8**

Table 1 (continued)

Acceptor	Donor	Ratio	Structure
Pt 1	**N5**	1 + 1 + 1 + 4	**Metallacycle M9**
	N9		
	N4		

with PEG chains (**Pt5**) was synthesized. **M34/35**[39,40] were prepared in high yields by combining 120° precursor **N18/30** and **Pt5**.[39,40] Treating **Pt6/7** with **N31** in $CH_2Cl/DMAc$ for 24 h at 60 °C resulted in the formation of triangular metallacycles **M36/37**.[69]

As shown in Table 5, rhomboid **M38**[70] was obtained by mixing donor **N32** with acceptor **Pt8**.[70] Products **M38–42** were obtained by precipitation and redissolved in DMSO. A 120° TPE-based dipyridyl ligand, **N11**, and **Pt8** were combined to furnish hexagonal **M39**,[65] and its optical properties were evaluated.[65] To obtain additional Pt-based compounds, a Pt(IV) prodrug was covalently conjugated to a 120° dipyridyl building block (**N33**). Subsequently, **N33** self-assembled with **Pt8** and generated supramolecular hexagonal **M40**.[71]

M41[72] was prepared by mixing donor **N34** with **Pt8** at the appropriate stoichiometry.[72] To enhance the photosensitization efficiencies and catalytic activities, **N35** was designed and mixed with **Pt8** to afford metallacycle **M42**.[73]

As shown in Table 6, stirring **N36/N32** and **Pt8** in CH_2Cl_2/acetone led to the formation of [1 + 2 + 4] double rhomboid **M43**.[70] Tris-[2]pseudorotaxane metallacycle **M44**[74] was obtained by the interaction between **Pt9** and **N37**.[74] **M45/46**[75] were obtained by combining **Pt9** and **N17/38**.[75]

At room temperature, hexagonal **M47**[76] was prepared by stirring a mixture of **Pt10** and linear donor **N39** in acetone-d^6 for 8 h.[76] As shown in Table 7, the [3 + 3] assembly of 120° diplatinum acceptor **Pt11** with 120° donor **N10/11** gave hexagonal **M48/49**.[64,65] Hexagonal metallacycle **M50**[77] was prepared by stirring a mixture of **N40** and **Pt11** in CH_2Cl_2 and CH_3OH.[77] Hexagonal metallacycle **M51**[67] was furnished by mixing alanine-based donor **N29** and **Pt11** in a 1:1 molar ratio.[67] **M52**[78] was obtained from **N41** and **Pt11** and was characterized by various spectroscopic techniques.[78] Ditopic, Ru(II)-containing donor **N42** was obtained by replacing one of the bpy groups of $Ru(bpy)_3^{2+}$ with 4,4′:2′,2″:4″,4″′-quaterpyridine. The combination of **N42** with **Pt12** in CH_2Cl_2/CH_3OH resulted in the formation of [2 + 2] rhomboid **M53**.[79]

As shown in Table 8, hexagonal metallacycle **M54**[72] was prepared via a combination of 120° donor **N34** and acceptor subunit **Pt13**.[72] **M55**[80] was prepared by mixing methyl viologen-modified dipyridyl donor **N43** and 120° platinum(II) acceptor **Pt14** in a mixture of H_2O and acetone at room temperature

Table 2 Pt1–2 (anion: ONO_2^-/OTf)-based rhomboids (**M10–14**)

Acceptor	Donor	Ratio	Structure
Pt 1	N10	2 + 2	Metallacycle M10
	N11	2 + 2	Metallacycle M11
	N12	2 + 2	Metallacycle M12
Pt 2	N13	2 + 2	Metallacycle M13
	N14	2 + 2	Metallacycle M14

Table 3 Pt3-based rhomboids (**M15–29**)

Acceptor	Donor		Ratio	Structure
	N11		2 + 2	Metallacycle M15
	N15		2 + 2	Metallacycle M16
	N16		2 + 2	Metallacycle M17
Pt 3		R_1 / R_2		
	N17	H / H		
	N18	NH_2 / H		
	N19	H / NH_2		
	N20	NH_2 / NH_2	2 + 2	Metallacycle M18-M25
	N21	NO_2 / NH_2		
	N22	COOMe / NH_2		
	N23	Me / NH_2		
	N24	$PhCH_3$ / NH_2		
		R		
	N25	NH_2		
	N26	H	2 + 2	Metallacycle M26-M29
	N27	OH		
	N28	OCH_3		

for 12 h followed by anion exchange.[80] Stirring mixtures of coumarin-functionalized 120° dipyridyl donor **N44**, AgOTf and 120° di-Pt(II) acceptors **Pt15/16** in CD_2Cl_2 at room temperature for 8 h led to the formation of hexagonal metallacycles **M56/57**, respectively.[81]

M58[82] was obtained by mixing linear donor **N45** with Pt acceptor **Pt17**.[82] Analogous macrocycle **M59**[82] was synthesized from donor 1,4-di(4-pyridylvinyl)benzene **N46**.[82] **N47/35**, 120° donor ligands without and with a porphyrin moiety, are well-known $^1O_2$ photosensitizers and were mixed with ligand **Pt18** to afford discrete metallacycles **M60/61**.[83]
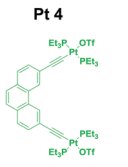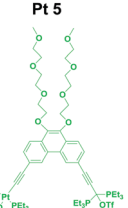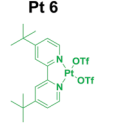
As shown in Table 9, **M62**[84] was generated by stirring B21C7-tethered acceptor **Pt19** and UPy-decorated donor **N13** at a 1 : 1 molar ratio for 6 h in a mixture of CD_2Cl_2 and CD_3NO_2.[84] Stirring a 1 : 1 mixture of methyl viologen-modified 120° donor **N43** and 120° platinum(II) acceptor **Pt20** in H_2O and acetone mixture at room temperature, followed by anion exchange, resulted in the formation of hexagonal **M63**.[85]

Chiral donor **N48** and Pt(II) nitrate **Pt21/22** were stirred in a mixed solvent for 8 h at 55 °C, and saturated KPF_6 solution was added. Then, **M64/65**[86] were prepared by recrystallization from a mixture of CH_2Cl_2 and ethyl ether.[86] **M66–68**[87,88] were obtained by stirring a mixture of **N11** with **Pt23–25** in CD_2Cl_2 at room temperature.[87] **M69**[89] was prepared from BODIPY dye-based building blocks **N49** and **Pt26** and characterized.[89]

As shown in Table 10, organic ligand **N50** and 180° acceptor **Pt27** were mixed in acetone at 30 °C for 2 h to generate **M70**.[90] Mixing ligands **N51** and **Pt27** in acetone for 4 h at room temperature afforded **M71** with pendant pyrene moieties.[91] **M72** was obtained from mixing clip donors **N7** and **Pt27** at 55 °C.[63] **M73**[92] was prepared by mixing donor ligand **N6** with **Pt27** in a mixed solvent of acetone and water.[92]

To study the influence of metallacycle shape on the optical properties, 120° TPE-based ligand **N11** was combined with **Pt27** to furnish rhomboid **M74**.[65] To compare the shape effects of

Table 4 Pt4–7-based metallacycles (M30–37)

Acceptor	Donor	Ratio	Structure
Pt 4	N10	2 + 2	Metallacycle M30
	N29	2 + 2	Metallacycle M31
	O1	2 + 2	Metallacycle M32
	O2	3 + 3	Metallacycle M33
Pt 5	N18	2 + 2	Metallacycle M34
	N30	2 + 2	Metallacycle M35
Pt 6	N31	3 + 3	Metallacycle M36
Pt 7		3 + 3	Metallacycle M37

Table 5 Pt8-based metallacycles (M38–42)

Acceptor	Donor	Ratio	Structure
Pt 8	N32	2 + 2	Metallacycle M38
	N11	3 + 3	Metallacycle M39
	N33	3 + 3	Metallacycle M40
	N34	3 + 3	Metallacycle M41
	N35	3 + 3	Metallacycle M42
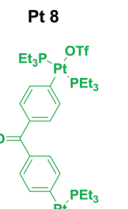
triangles and rhomboids, triangular **M75** was obtained by mixing donor **N32** with **Pt27**.[70] **M76** was synthesized by mixing donor **N7** with **Pt28**.[75] As shown in Table 11, **N52** was mixed with 180 Pt(II) compound **Pt27** in DMSO for 5 h at 80 °C to obtain **M77**.[93] Mixing **N36**, **N32** and **Pt27** in CH$_2$Cl$_2$/acetone led to the formation of [1 + 4 + 6] double triangle **M78**.[70]

N52 was mixed with **Pt29** in a 1 : 2 ratio in DMSO at 80 °C to obtain **M79**.[93] Functionalized metallacycles **M80/81**,[62] containing alkynyl-Pt(II) bzimpy moieties, were then prepared by mixing **N6** with **Pt29/30** in acetone/water at 55 °C.[62] TPE-based ligand **N11** was combined with **Pt31** to furnish rhomboid **M82**.[65]

M83/84[59] were prepared in one pot *via* a two-component CDSA by stirring ligand **O1** with either 180° Pt-based acceptor **Pt27** or **Pt31** in a 1 : 1 ratio.[59] **M85**[77] was prepared by stirring a mixture of **N40** and **Pt32** in CH$_2$Cl$_2$/CH$_3$OH for 10 h.[77] **M86**[78] was obtained from **N41** and Pt-acceptor **Pt32** in a mixed solvent system of dichloromethane–methanol for 6 h at room temperature (Table 12).[78]

As shown in Table 13, molecular squares **M87–90**[43] were obtained from 4,4′-bipyridine and **N38**, **N53–55** and **Pt33** by using the ball milling method.[43] **M91**[94] was obtained by treating

Pt7 with an equimolar amount of donor **N56** in freshly distilled dichloromethane under continuous stirring at 50 °C for 24 h.[94] **M92** was obtained by treating linear donor **N45** with **Pt34**.[82] Analogue **M93** was generated by using 1,4-di(4-pyridylvinyl)benzene **N46**.[82] **M94**[89] was prepared from BODIPY dye-based building blocks **N49** and **Pt35** and characterized.[89] **M95** was fabricated from **N57** and **Pt36** and characterized.[95]

Rhomboid **M96** was furnished by stirring ligand **O1** with **Pt7** in a solution of H$_2$O/CD$_3$COCD$_3$ and then CD$_3$COCD$_3$.[59] By stirring paraquat-derived carboxylate ligand **O2** and **Pt7** and dipyridyl ligands **N54/58** in a 1 : 2 : 1 ratio in H$_2$O/acetone, squares **M97/98** were obtained.[68] Rectangular compounds **M99–101** were prepared *via* a three-component CDSA strategy.[44] **N59** and one of dicarboxylates **O3–5** were mixed with **Pt7** in acetone/water. The desired product was obtained by ethyl ether-induced precipitation. Huang reported the construction of two anthracene-based rectangles, **M102** and **103**,[96] by means of CDSA with **Pt7** and organic donor **N45** and dicarboxylates **O6** and **7**, respectively.[96] Ligand **N60**; dicarboxylate donors **O4**, **O8**, **O9**, **O10** and **O3** with different bite angles

Table 6 **Pt8–10**-based metallacycles (**M43–47**)

Acceptor	Donor	Ratio	Structure
Pt 8	**N36** / **N32**	1 + 2 + 4	Metallacycle **M43**
Pt 9	**N37**	3 + 3	Metallacycle **M44**
	N17	3 + 3	Metallacycle **M45**
	N38	6 + 6	Metallacycle **M46**
Pt 10	**N39**	6 + 6	Metallacycle **M47**

Table 7 **Pt7–12**-based rhomboids (**M48–53**)

Acceptor	Donor	Ratio	Structure
	N10	3 + 3	Metallacycle **M48**
	N11	3 + 3	Metallacycle **M49**
Pt 11	**N40**	3 + 3	Metallacycle **M50**
	N29	3 + 3	Metallacycle **M51**
	N41	3 + 3	Metallacycle **M52**
Pt 12	**N42**	2 + 2	Metallacycle **M53**

between the carboxylate groups; and **Pt7** were mixed in a molar ratio of 1 : 1 : 2 to produce **M104–108** (Table 14).[46]

As shown in Table 15, **M109–111** were obtained by mixing **Pt37** with **O6**, **O7** and **O11**.[97] **M112–113** were obtained by mixing **Pt38** and **N38** and **N61**.[98] Pyridine-terminated molecular rectangles **M114–115** were obtained from **Pt39** and **N53** and **57**.[45]

2.2 Metallacages

As shown in Table 16, metallacage **G1** was prepared from **N61/62** and **Pt40**.[99] Metallacage **G2** was obtained from **N62/O11** and **Pt7**.[50] Metallacage **G3** was synthesized from **N56/62** and **Pt7**.[94] Chiral *cis*-[(1S,2S)-dch]Pt(NO$_3$)$_2$ (**Pt41**) and a hexadentate ligand (**N63**) assembled to form chiral M$_{12}$L$_4$ molecular tetrahedron **G4**.[100] **G4** possesses an internal nanocavity, which allows it to catalyse Michael addition reactions of nitrostyrene derivatives.

The self-assembly of the tris(pyridyl)borane donor **N64** with platinum (**Pt7**) and diruthenium (**Ru1**) electron acceptors furnished boron-containing trigonal prismatic supramolecular metallacages **G5/6**.[48] Zhang described the preparation of molecular-clip-based tetrapyridyl donors (**N65/66**) and subsequently used them to synthesize four trigonal-prismatic cages (**G7–10**) by CDSA with 180° platinum(II) acceptors (**Pt32/42**).[49] Hor and co-workers assembled a series of triangular metallaprisms (**G11**) with functional [Pt(HL)]-corner units (**Pt43**) using different coordination sequences.[51]

Yan *et al.* reported the fabrication of the tetragonal metallacage (Table 17) **G12**.[53,56,101] Then, four metallacages (**G13–16**)[54] with tuneable properties were prepared by the assembly of **O12–15** bearing various substituents with **N36**, and **Pt7**.[54] Upon mixing **Pt7** and carboxylate ligand **O6** with

3894 | Chem. Soc. Rev., 2020, 49, 3889–3919

This journal is © The Royal Society of Chemistry 2020

Table 8 **Pt13–18**-based metallacycles (**M54–61**)

Acceptor	Donor	Ratio	Structure
Pt 13	**N34**	3 + 3	Metallacycle **M54**
Pt 14	**N43**	3 + 3	Metallacycle **M55**
Pt 15 / **Pt 16**	**N44**	3 + 3	Metallacycle **M56-M57**
Pt 17	**N45**	6 + 6	Metallacycle **M58**
	N46	6 + 6	Metallacycle **M59**
Pt 18	**N47**	3 + 3	Metallacycle **M60**
	N35	3 + 3	Metallacycle **M61**

Table 9 **Pt19–24**-based metallacycles (**M62–69**)

Acceptor	Donor	Ratio	Structure
Pt 19	**N13**	3 + 3	Metallacycle **M62**
Pt 20	**N43**	3 + 3	Metallacycle **M63**
Pt 21	**N48**	2 + 2	Metallacycle **M64**
Pt 22		2 + 2	Metallacycle **M65**
x = NO₃ **Pt 23** / x = OTf **Pt 24** / x = PF₆ **Pt 25**	**N11**	3 + 3	Metallacycle **M66-M68**
Pt 26	**N49**	2 + 2	Metallacycle **M69**

N36 in a specific ratio, an equilibrium with supramolecular prism (**G17**) as the predominant species was obtained.[102] The combination of **N36**, poly(ethylene glycol) (PEG)-decorated dicarboxylate ligand **O16** and **Pt7** resulted in the formation of discrete tetragonal metallacage **G18**.[56] When two donor building blocks (**O17** and **N36**) were mixed with **Pt7** in the appropriate solvents, metallacage **G19** was formed.[103] **G20** was obtained from mixing **O1**, **Pt7** and **N36** in a ratio of 4 : 8 : 2 in H_2O/CD_3COCD_3 followed by CD_3COCD_3.[59]

Metallacages **G21/22** were obtained by stirring a mixture of **Pt23–25** with **N36** in a 2 : 1 ratio at 50 °C.[87] The OTf⁻ anion of cage **G22** was exchanged by treatment with a saturated aqueous solution of KPF₆ to yield **G23**.[87] **G24** was prepared from the self-assembly of TPE-based ligand **O18**, **Pt7**, and 21-crown-7

appendant dipyridyl ligand **N67**.[55] To investigate the influence of pillars on emissive properties, Zhang synthesized three emissive tetragonal prisms, **G25–27**, consisting of eight **Pt7** and three dipyridyl ligands (**N38**, **68** and **69**).[57] In addition to TPE, porphyrin can be used as faces to construct tetragonal prisms. For example, **G28** was prepared by mixing **Pt7**, carboxylate ligand **O6** and **N70** in a ratio of 8 : 4 : 2.[52,104] Upon formation of **G29–30**,[104] the intermolecular π–π stacking of TPP (5,10,15,20tetra(4-pyridyl)porphyrin) was effectively suppressed, and significant enhancements of the fluorescence and $^1O_2$ generation quantum yield were realized.[104] **G31** was obtained by the CDSA of **N70** with **O1**,[59] and **G32** was obtained by the CDSA of **N36** with **N38**.[95]

Chen and Yu loaded octaethylporphine (OEP) in to hexagonal metallacage (**G33**)[58] to form multifunctional system **G33** ⊃ OEP, which was wrapped to afford nanoparticles (MNPs).[58] As shown in Table 18, **G33**[59] was quantitatively prepared from three

This journal is © The Royal Society of Chemistry 2020

Chem. Soc. Rev., 2020, **49**, 3889–3919 | **3895**

Table 10 Pt27–28-based metallacycles (M70–76)

Acceptor	Donor	Ratio	Structure
Pt 27	N50	2 + 2	Metallacycle M70
	N51	2 + 2	Metallacycle M71
	N7	2 + 2	Metallacycle M72
	N6	2 + 2	Metallacycle M73
	N11	6 + 6	Metallacycle M74
	N32	3 + 3	Metallacycle M75
Pt 28	N7	6 + 6	Metallacycle M76

Table 11 Pt27–31-based metallacycles (M77–82)

Acceptor	Donor	Ratio	Structure
Pt 27	N52	6 + 6	Metallacycle M77
	N36	6 + 1 + 4	Metallacycle M78
	N32		
Pt 29	N52	6 + 6	Metallacycle M79
Pt 29 / Pt 30	N6	2 + 2	Metallacycle M80–M81
Pt 31	N11	3 + 3	Metallacycle M82

Hexagonal prismatic macrocycles G38–39[107] were obtained from the [6 + 12] CDSA of ~120° donors (N75/76) with Pt7 in a 1:2 ratio.[107] G40–42 were obtained by the [3 + 6] assembly of N77/78/79 with Pt44.[95] To improve the binding affinity and selectivity towards specific DNA topologies, Terenzi reported three Pt(II) dinuclear squares (G43–45)[108] and their constituent L-shaped 4,4′-bipyridine ligands N80–N82 as DNA binders.

As shown in Table 20, G46 and 47 were obtained by the assembly of N77/78 with Pt44.[95] G48 was obtained by the [24 + 24] assembly of N52 with palladium.[93] Cao also reported a direct method to construct two diamondoid based frameworks (G49–50) from N83 as a node and two linear platinum(II) acceptors (Pt27/31) as linkers,[60] resulting in the formation of periodic and porous structures. G51 was obtained by the assembly of N83 with Pt8.[61] Zhou described the use of molecular self-assembly to prepare a metallacage with strong 2-photon absorption by combining multiple Ru(II) complexes with Pt(II) building blocks via CDSA. The combination of N42 with tri-Pt(II) acceptor Pt45 in CH_2Cl_2/CH_3OH (v/v = 1/1) resulted in the formation of [6 + 4] octahedral metallacage G52.[79] Pt_6L_4 cage G53 was made by combining N62 with

species, namely, hexakis[4(4pyridylethynyl)phenyl]benzene (N73), disodium terephthalate (O6), and Pt7, in a 2:6:12 ratio.[59] Hexagonal prism G34 was prepared from O1, Pt7 and hexapyridyl compound N73 in a ratio of 6:12:2. Taking advantage of the pyridyl groups, the CDSA of N74 with 60° diplatinum species Pt2 in an appropriate ratio led to the formation of G35.[105]

He et al. described the preparation and characterization of G36–37 with potential light-harvesting properties (Table 19).[106] These complexes were obtained from the self-assembly of Pt7 with 5,10,15,20-tetra(4-pyridyl)-21H,23H-porphine (N70) or 2,4,6-tris(4-pyridyl)-1,3,5-triazine (N62).

3896 | Chem. Soc. Rev., 2020, 49, 3889–3919

This journal is © The Royal Society of Chemistry 2020

Table 12 Pt27–32-based metallacycles (**M83–86**)

Acceptor	Donor	Ratio	Structure
Et₃P–Pt–PEt₃ OTf ≡ Et₃P–Pt–PEt₃ OTf n = 1 **Pt 27** n = 2 **Pt 31**	**O1** COONa O O COONa	4 + 4	**Metallacycle M83-M84**
Pt 32 Et₃P Pt OTf PEt₃ Et₃P Pt PEt₃ OTf	**N40**	6 + 6	**Metallacycle M85**
	N41	6 + 6	**Metallacycle M86**

Table 13 Pt33–36-based metallacycles (**M87–95**)

Acceptor	Donor	Ratio	Structure
Pt 33 H N Pt Cl Cl H N	**N38**	4 + 4	**Metallacycle M87**
	N53	4 + 4	**Metallacycle M88**
	N54	4 + 4	**Metallacycle M89**
	N55 HO O O OH	4 + 4	**Metallacycle M90**
Pt 7 Et₃P Pt OTf Et₃P OTf	**N56**	4 + 4	**Metallacycle M91**
Pt 34 O₃N PEt₃ Et₃P Et₃P PEt₃ O₃N	**N45**	4 + 4	**Metallacycle M92**
	N46	4 + 4	**Metallacycle M93**
Pt 35 TfO PPh₃ Ph₃P Pt B Ph₃P Pt PPh₃ TfO Pt Ph₃P	**N49**	2 + 2	**Metallacycle M94**
Pt 36 Ph P—Ph Pt²⁺ Ph P Ph	**N57**	4 + 4	**Metallacycle M95**

tri-Pt(II) acceptor **Pt46**.[109] **G54** was prepared by the coordination of **N84** and palladium/platinum.[110–112]

3. Characterization

In addition to the routine use of NMR spectroscopy, X-ray crystallographic analysis and ion mobility mass spectrometry play an important role in CDSA.
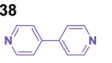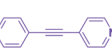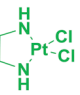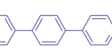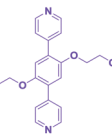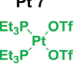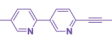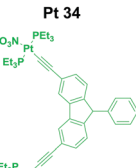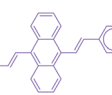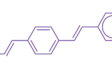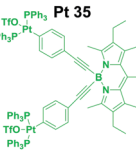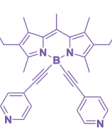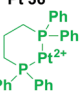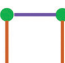
3.1 X-ray crystallographic analysis

As shown in Fig. 1a, to confirm the conformation of **M73**,[92] a model metallacycle (MM) was designed and prepared. Through the slow evaporation of MM CH_2Cl_2 solution, white crystals were obtained, revealing that MM adopted a chair conformation in the solid state. Crystals of **M70**[90] were prepared by slow diffusion, and they were structurally characterized by X-ray diffraction (Fig. 1b). Slow diffusion of ether into an acetone solution of **M71** afforded light-yellow single crystals of **M71**[91] (Fig. 1c). Crystallographic analysis revealed the formation of an AA–BB-type monomer composed of two molecules of **M71** connected by C–H···π interactions.

The slow diffusion method was also used to obtain single crystals of **M1** and **M2** (Fig. 2).[36] The side view of the crystal showed that the metallacycle was essentially planar with four triethylphosphine ligands perpendicular to the metallacycle plane.

The X-ray crystal structure of **G4** is shown in Fig. 3.[100] Vapor diffusion of acetone into a water/methanol solution of **G4** afforded single crystals of **G4**. Chiral triangular subunits are present at the four corners of the tetrahedron, making **G4** chiral.

X-ray crystal analysis clearly show the molecular structure and connectivity of **G6**.[48] The cation of **G6** was confirmed to be a hexanuclear ruthenium trigonal prismatic supramolecular cage consisting of six half-sandwich Ru units and two borane ligands with an interior pocket of approximately 400 Å³, as estimated using the six Ru vertices. Notably, the propeller-like conformation of the two triarylborane units prevented π-stacking interactions between these units (Fig. 4).

Pale-yellow crystals of **G54**·5EO (ethylene oxide) were prepared by slow concentration of the saturated H_2O solution for 1 month at room temperature (Fig. 5a and b).[112] The bound

This journal is © The Royal Society of Chemistry 2020

Chem. Soc. Rev., 2020, **49**, 3889–3919 | **3897**

Table 14 Pt7-based metallacycles (**M96–108**)

Acceptor	Donor	Ratio	Structure
	O1 COONa, OMe, OMe, COONa	2 + 2	Metallacycle **M96**
	N54		
	N58	4 + 2 + 2	Metallacycle **M97-M98**
	O2		
	N59	4 + 2 + 2	Metallacycle **M99-M101**
	O3 COOK, **O4** COOK, **O5** COOK	4 + 2 + 2	
Pt 7 Et3P, Pt, OTf, Et3P, OTf	**N45**	4 + 2 + 2	Metallacycle **M102-M103**
	O6 NaO2C, **O7** NaO2C		
	N60	1 + 1	Metallacycle **M104-M108**
	O4 COOK, **O8** COOK, **O9** COOK, **O10** COOK, **O3** COOK		

Table 15 Pt37–39-based metallacycles (**M109–115**)

Acceptor	Donor	Ratio	Structure
Pt 37	**O6**, **O7**, **O11**	2 + 2	Metallacycle **M109-M111**
Pt 38	**N38**	2 + 2	Metallacycle **M112-M113**
	N61		
Pt 39	**N53**	2 + 2	Metallacycle **M114-M115**
	N57		

5EO adopts an approximately coiled conformation in the cavity (Fig. 5c). The optimized structure of **G54·CE** indicates that cyclic CE adopts a bent conformation to fit in the spherical cavity (Fig. 5d).

3.2 Ion mobility mass spectrometry

Although X-ray crystal analysis is a powerful tool for determining complicated structures, growing suitable crystals can be challenging.[95] In this case, ion mobility mass spectrometry (IM-MS) can provide a direct measure of the size and stoichiometry of these complexes.[113,114]

This approach obviates the need for product isolation and crystallization and allows the tracking of the product distribution over time. As shown in Fig. 6, the IM drift times do not change as a function of collision voltage, and each ion can be fit to a single Gaussian distribution throughout the collisional activation (CID) experiment; therefore, ions are observed to dissociate rather than rearrange or unfold in the gas phase.[114]

The ESI-MS data of **M77** showed a series of peaks as a result of the loss of different numbers of triflate counterions (Fig. 7a).[93] Furthermore, IM-MS showed a series of charge

states with a narrow drift-time distribution, thus confirming the structure (Fig. 7b).

For **G48**, ESI-MS gave a set of peaks with sequential charges (Fig. 8).[93] After deconvolution, the measured molecular weight of **G48** was confirmed.

IM-MS showed one dominant series of bands for each charge state with a narrow drift time. Travelling wave ion mobility-mass spectrometry (TWIM-MS) of **G38** and **G39** provides further evidence for the formation of the target structures. As shown in Fig. 9, the TWIM-MS data of **G38** and **G39** show a prominent set of signals with multiple charged states.[107]

4. Properties

The design, synthesis, and characterization of MOCs have been discussed above. The photophysics and photochemistry of MOCs are highly diverse, and small modifications in the ligands can result in changes in the molecular congener systems.[31–33] To better understand the resultant properties, the role of the bite angle, substituents, shape and size of the MOCs as well as the anions were investigated.

4.1 Optical properties

4.1.1 Bite angle and substituent effects. By systematically using dicarboxylate building blocks, phenazine-cored metallacycles **M104–108** were obtained.[46] As the metallacycle size decreased, the emission blueshifted (570 to 499 nm). The results indicate that the size of **M104–108** dictated the constraint imposed on the excited-state planarization of the core, thereby altering their photophysical properties (Fig. 10).

3898 | Chem. Soc. Rev., 2020, **49**, 3889–3919

This journal is © The Royal Society of Chemistry 2020

Table 16   Trigonal prisms (G1–11)

Acceptor	Donor	Ratio	Structure
Pt 40	N62 / N61	6 + 2 + 3	Metallacage G1
Pt 7	N62 / O11	6 + 2 + 3	Metallacage G2
Pt 7	N62 / N56	3 + 2	Metallacage G3
Pt 41	N63	12 + 4	Metallacage G4
Pt 7	O6	3 + 3	Metallacage G5
Ru 1	N64	3 + 3	Metallacage G6
Pt 32	N65 / N66	6 + 3	Metallacage G7–G8
Pt 42	N65 / N66	6 + 3	Metallacage G9–G10

Table 16   (continued)

Acceptor	Donor	Ratio	Structure
Pt 43	N38	2 + 3	Metallacage cis and trans G11

By selectively combining TPPE (N36), dicarboxylate moieties (O12–15), and Pt7, a series of metallacages (G13–16) with adjustable optical properties were prepared.[54] When the substituents were changed from –SO3Na to –NH2, the cage emission was brighter (Fig. 11).

Three Pt(II) rhomboidal metallacycles with orange (M15), cyan (M16), and green (M17) emissions were prepared.[41] As the concentration decreased, the emission of the assemblies formed by metallacycle M15 and a bis-ammonium linker shifted from orange to blue. White-light emission was obtained at a concentration of 29 μM (Fig. 12).

Yin prepared supramolecular polymers with tuneable fluorescence by CDSA and host–guest interactions.[37] By varying the substituents (N17–24) on the dipyridyl donors, the metallacycles exhibited emission wavelengths from 427 to 593 nm. White-light-emitting LED can be prepared by the combination of a thin film onto an ultraviolet LED and as-prepared MOCs (Fig. 13).

White-light emission from a single chromophore was realized by dissolution of G18 in THF.[56] The mixed yellow and blue emissions from the monomeric and aggregate ensembles resulted in overall white light (Fig. 14).

4.1.2   Effects of shape, size, and anion. In addition to the effects of bite angle and substituents, the shape of the metallacycles also plays an important role in tuning the emission.

Yan prepared a suite of TPE-based metallacycles (M10, 49, 39, 74, and 82) and used them as chemosensors (Fig. 15).[65] Because of their AIE characteristics, M10, M49 and M82 were explored for the detection of picric acid. Zhou described the selective formation of a metallarhomboid (M43) and a triangle (M75) by controlling the shape and stoichiometry of the ligand.[70] Differences in the strength and shape result in different fluorescence enhancement behaviours for the double rhomboid (M43) and double triangle (M78). Fused M43 showed weaker emission in dilute solutions. However, a reversal of emission intensities was observed in the aggregated state.[70] The different shapes result in dramatically different fluorescence efficiencies (Fig. 16).

N36 were used to construct M66–68 and drum-like metallacages (G21–23) with three different counteranions via CDSA.[87] A counterion effect was observed; compared with their NO3$^-$ counterion analogues, the species containing OTf$^-$ or PF6$^-$ counterions show stronger emission. The absorption coefficients, emission intensities, and quantum yield values in CH2Cl2 follow the order PF6$^-$ > OTf$^-$ > NO3$^-$ (Fig. 17).
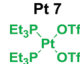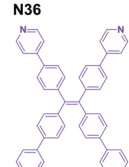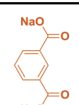
Table 17 Tetragonal prisms (**G12–32**)
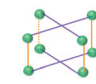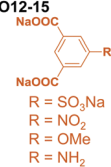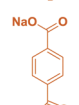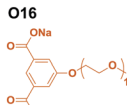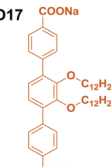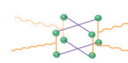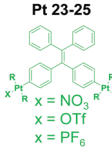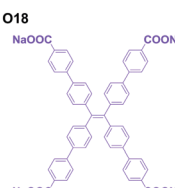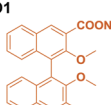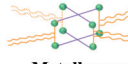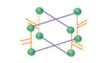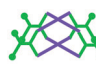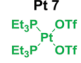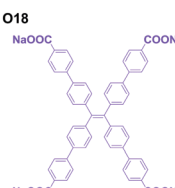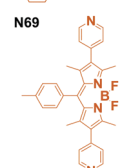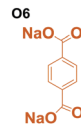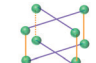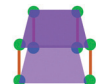
Acceptor	N-Donor	O-Donor	Ratio	Structure
Pt 7 Et₃P, OTf, Pt, Et₃P, OTf	N36	O7 NaO, O, NaO, O	8 + 2 + 4	
		O12-15 NaOOC, R, NaOOC, R = SO₃Na, R = NO₂, R = OMe, R = NH₂	8 + 2 + 4	Metallacage G12-G17
		O6 NaO, O, NaO, O	8 + 2 + 4	
		O16 ONa, O, (O)₁₅, ONa	8 + 2 + 4	Metallacage G18
		O17 COONa, O-C₁₂H₂₅, O-C₁₂H₂₅, COONa	8 + 2 + 4	Metallacage G19
		O1 COONa, O, O, COONa	8 + 2 + 4	Metallacage G20
Pt 23-25 R Pr x = NO₃ x = OTf x = PF₆			4 + 2	Metallacage G21-23

Acceptor	N/O-Donor	N-Donor	Ratio	Structure
Pt 7 Et₃P, OTf, Pt, Et₃P, OTf	O18 NaOOC, COONa, NaOOC, COONa	N67	8 + 2 + 4	Metallacage G24
		N38	8 + 2 + 4	
		N68	8 + 2 + 4	Metallacage G25-27
		N69	8 + 2 + 4	
	O6 NaO, O, NaO, O	N70	8 + 2 + 4	Metallacage G28

3900 | *Chem. Soc. Rev.*, 2020, **49**, 3889–3919

This journal is © The Royal Society of Chemistry 2020

Table 17 (*continued*)
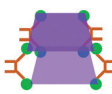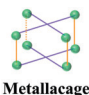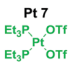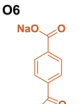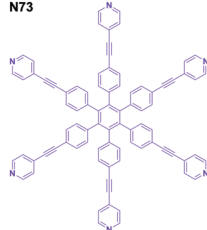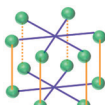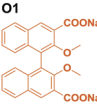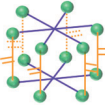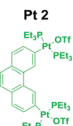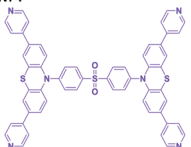
Acceptor	N/O-Donor	N-Donor	Ratio	Structure
		N71 (M = Cu) **N72 (M = Mn)**	8 + 2 + 4	**Metallacage G29-G30**
	O1 COONa COONa	**N70**	8 + 2 + 4	**Metallacage G31**
	N38	**N36**	8 + 2 + 4	**Metallacage G32**

Table 18 Hexagonal prisms and others (**G33–35**)

Acceptor	O-Donor	N-Donor	Ratio	Structure
Pt 7 Et₃P Pt OTf Et₃P OTf	**O6** NaO O O ONa	**N73**	12 + 6 + 2	**Metallacage G33**
	O1 COONa COONa			**Metallacage G34**
Pt 2 Et₃P Pt OTf PEt₃ PEt₃ Pt OTf Et₃P		**N74**	4 + 2	**Metallacage G35**

Liu assembled **G11** using different coordination sequences. By utilizing Pt–N bonds and the trans effect of a carbon donor, they successfully tuned the luminescence of geometric isomers of metallosupramolecules (Fig. 18).[51]

4.1.3 Observation and understanding of CDSA emission. Han prepared fullerene-functionalized metallacycle **M72** (Fig. 19) and explored its excited-state decay pathways in a concentrated solution and showed that a radiative excimer with a long-lived triplet state can exist in a concentrated solution of fullerene–Pt complex.[115]

Investigating the origin of changes in absorption and emission properties is important for understanding the photophysical nature and electronic structure of MOCs. As shown in Fig. 20, self-assembly into **G35**[105] increases the quantum yield in solution 4-fold primarily due to the further twisting of the luminophore, which increases the radiative rate constant. The differences in quantum yields can be explained by the twist

in the chromophore upon coordination to platinum or methylation of the pyridyl group, leading to intersystem crossing to a triplet state.[105] This state then becomes more emissive with the addition of platinum, which increases the radiative rate constant *via* the heavy atom effect.

4.2 Host–guest properties

Due to the cyclic nature of these compounds, metallacycles and metallacages often have a central space capable of binding guests. As a result, a wide range of guest molecules with different properties, including metal ions, C_{60}, pyrene, naphthalene, coronene, glucose, and oligo (ethylene oxides), have been successfully encapsulated in metallacycles and metallacages. As complex systems, the interactions between species give rise to one or more properties that cannot be attributed to their individual components.[16,116]

4.2.1 Metallacage cavities used as hosts. Han reported that the encapsulation of a chromophore by **G2** dramatically enhances its photophysical properties (Fig. 21).[50] Core-to-cage charge transfer (CCCT) arises from the electrostatic interactions between the delocalized electrons of the coronene and the positive charge associated with the metallacage. The Pt nodes of the host contribute to the excited-state frontier orbitals, further promoting intersystem crossing (ISC) and phosphorescence.

A similar **G1**-based system was investigated by combining several characterizations.[99] A mechanism revealing the main excited-state decay pathways was proposed (Fig. 22).

He described the design and synthesis of square-like **M91** and trigonal prismatic **G3** by precisely controlling the ratio between donor **Pt7** and two different acceptors.[94] **M91** and **G3** could selectively recognize divalent metal ions (Ni^{2+} and Zn^{2+}) over monovalent (Ag^+) or trivalent metal ions (Nd^{3+}, Eu^{3+} and Tb^{3+}), as shown in Fig. 23.

Zhang described the synthesis of four convex trigonal prisms **G7–10** *via* CDSA with 180° platinum(II) acceptors **Pt32/42**.[49] Because of the large flexible aromatic surfaces of these cages, their encapsulation of fullerene was investigated (Fig. 24).

This journal is © The Royal Society of Chemistry 2020

Chem. Soc. Rev., 2020, **49**, 3889–3919 | **3901**

Table 19 Trigonal, hexagon prisms (**G36–45**)

Acceptor	Donor	Ratio	Structure
Pt 7 Et₃P–Pt–OTf / Et₃P–OTf	**N70**	6 + 3	Metallacage **G36**
	N62	6 + 4	Metallacage **G37**
	N75	12 + 6	Metallacage **G38–G39**
	N76		
Pt 44 Me₃P–Pt–OTf / Me₃P–OTf	**N77**	6 + 3	Metallacage **G40–G42**
	N78		
	N79		
	N80		
Pt 40	**N81**	2 + 2	Metallacage **G43–G45**
	N82		

Table 20 Complicated cages (**G46–54**)

Acceptor	Donor	Ratio	Structure
Pt 44 Me₃P–Pt–OTf / Me₃P–OTf	**N77**	12 + 6	Metallacage **G46**
	N78	28 + 14	Metallacage **G47**
Pd 1 Pd(NO₃)₂	**N52**	24 + 24	Metallacage **G48**
Pt 27 n = 1 / **Pt 31** n = 2	**N83**	12 + 10	Metallacage **G49–50**
Pt 8		6 + 4	Metallacage **G51**
Pt 45	**N42**	6 + 4	Metallacage **G52**
Pt 46	**N62**	6 + 4	Metallacage **G53**
Pd 1 Pd(NO₃)₂	**N84**	2 + 4	Metallacage **G54**

DOSY results suggested that encapsulation does not alter the overall size of the cage.

Additionally, the host–guest interactions between **G28** and pyrene were investigated.[52] This recognition could be used to inhibit the liquid-crystalline behaviour of the nematic molecule containing cyanobiphenyl mesogens functionalized with a pyrenyl unit. Then, coronene was used as a competitive guest to recover the liquid-crystalline behaviour of the smectic material (Fig. 25).[52]

Chen and Yu utilized **G33**-containing therapeutic platinum(II) to encapsulate a photosensitizer, facilitating the codelivery of a chemotherapeutic agent and a photosensitizer (Fig. 26).[58] Benefiting from the enhanced permeability and retention, the nanomedicine exhibited satisfactory antitumour performance against drug-resistant tumours.

Yoshizawa reported the selective and efficient loading of D-sucrose within a molecular capsule (**G54**) from natural aqueous saccharide mixtures (Fig. 27).[111]

Multiple CH–π interactions between the sucrose hydrocarbon backbone and the shape-complementary polyaromatic cavity endow **G54** with unique selectivity, as demonstrated by theoretical calculations and control experiments. In addition, they disclosed unusual host–guest complexation between **G54** and long amphiphilic oligomers.[111] These unusual host–guest interactions occurred instantly, spontaneously, and quantitatively even in water at room temperature (Fig. 28).[112]

4.2.2 Metallacycle cavities used as hosts. Three metallacycles (**M11, 30,** and **48**) with controlled shapes and cavity sizes were generated by CDSA.[64] Metallacycles with finely tuned cavity sizes possess different degrees of flexibility to accommodate C₆₀. Upon host–guest complexation with C₆₀, the

3902 | Chem. Soc. Rev., 2020, **49**, 3889–3919
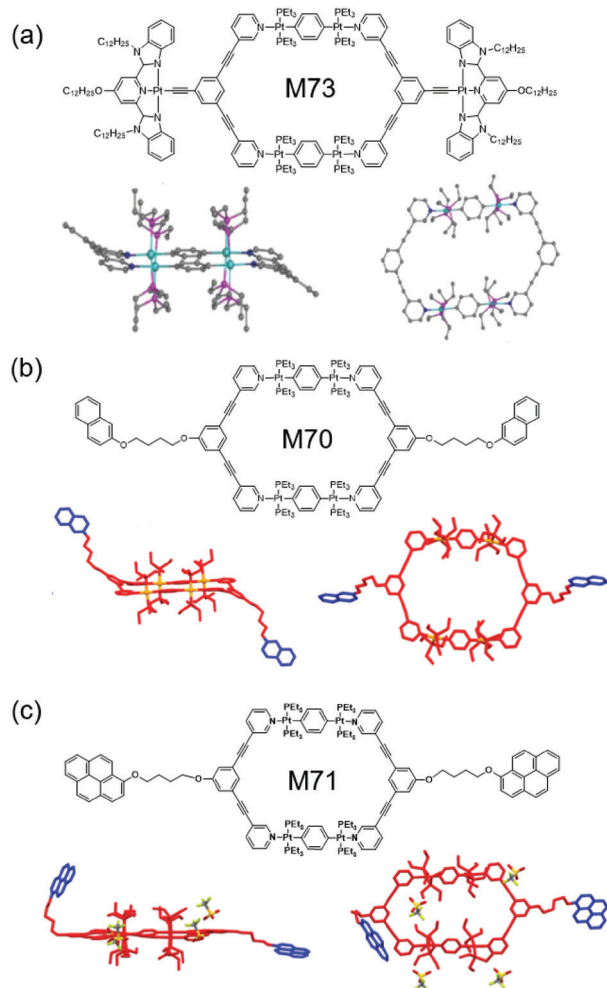
This journal is © The Royal Society of Chemistry 2020

Fig. 1 Chemical and crystal structures of (a) **M73**, (b) **M70** and (c) **M71**. Figure adapted from ref. 90–92 with permission from the American Chemical Society, Copyright 2018 and 2019.
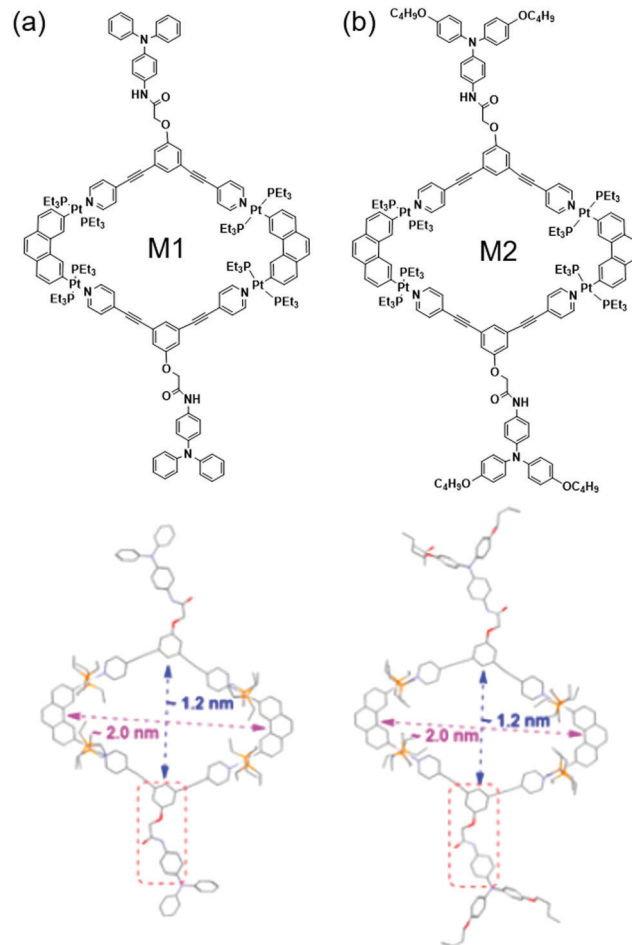

Fig. 2 Chemical and crystal structures of (a) **M1** and (b) **M2**. Figure adapted from ref. 36 with permission from the American Chemical Society, Copyright 2019.
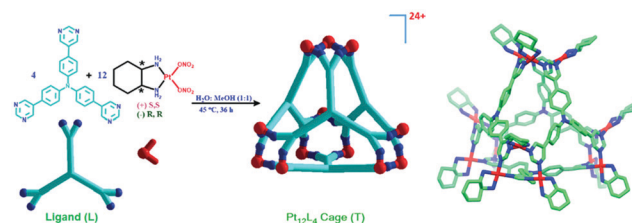

Fig. 3 Chemical and crystal structures of **G4**. Figure adapted from ref. 100 with permission from Royal Society of Chemistry, Copyright 2018.

molecular conductance of the metallacycle could be enhanced by an order of magnitude (Fig. 29).

Shi prepared metallacycle **M70** bearing two naphthalene units at its vertices, and it can be used to construct a linear supramolecular polymer through host–guest interactions between the cavity of the metallacycle and the naphthalene groups (Fig. 30).[90]

Then, metallacycle **M71** containing two pyrene units was synthesized (Fig. 31).[91] One of the pyrenes was encapsulated into the cavity of another pyrene of **M71** to form a host–guest complex. Both in the solid state and in solution, **M71** assembled into a supramolecular polymer.[91]

4.2.3 Functionalized pillars as hosts. Yin prepared new, bicyclic cross-linked supramolecular polymers by hierarchical unification of **M26–29**.[66] The B21C7 units in the vertical direction provide a platform for incorporating the host–guest interactions with bis-ammonium, affording a cross-linked supramolecular polymer network (Fig. 32).

Cross-linked redox-responsive supramolecular polymers can be formed based on host–guest interaction between a guest and a metallacycle **M44** (Fig. 33).[74]

Based on the host–guest interactions between **G24** and ammonium salts, Yin prepared a supramolecular gel with **G24** as the core by orthogonal self-assembly.[55] Due to the dynamic nature of the noncovalent interactions in this system, its thermo- and cation-responsiveness is well preserved (Fig. 34).

Recently, interlocked molecular species have attracted considerable attention because of their application as nanoscale devices and molecular machines. As shown in Fig. 35. Based on the host–guest interactions that occur in catenanes and molecular necklaces, mechanically interlocked molecules

This journal is © The Royal Society of Chemistry 2020

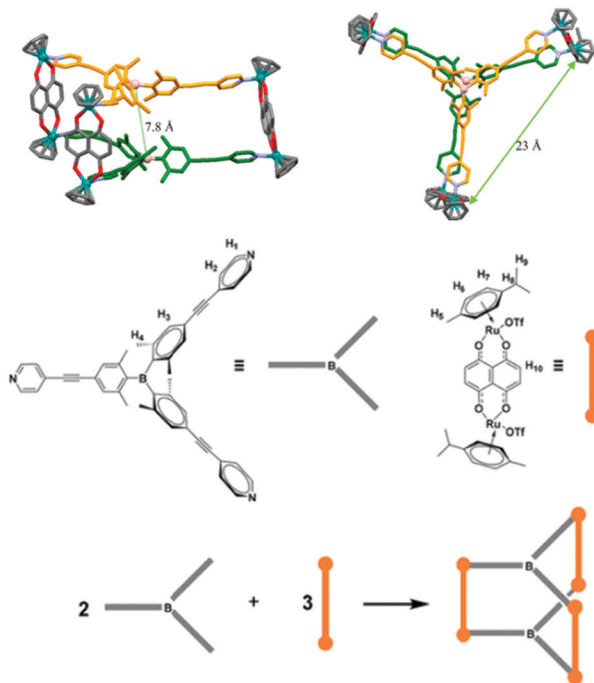Chem. Soc. Rev., 2020, **49**, 3889–3919 | **3903**

Fig. 4 Chemical and crystal structures of **G6**. Figure adapted from ref. 48 with permission from American Chemical Society, Copyright 2018.
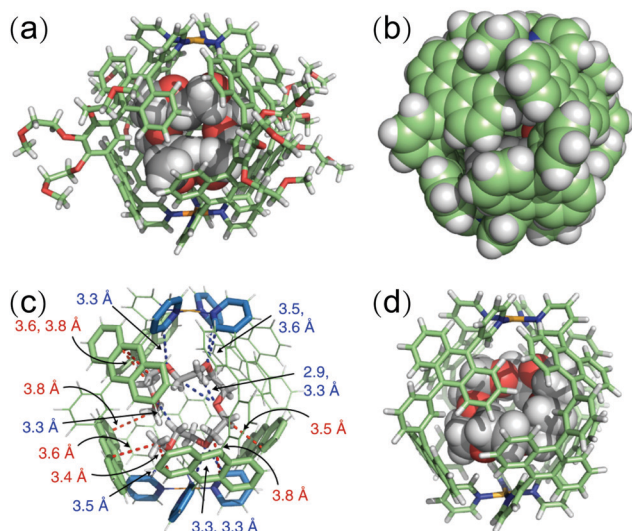

Fig. 5 Chemical and crystal structures of **G54** and guest. Figure adapted from ref. 112 with permission from Springer Nature, Copyright 2018.

consisting of two catenanes and one molecular necklace were efficiently constructed.[117]

4.3 Hierarchical assembly

MOCs with controllable shapes and sizes have been employed to construct hierarchical systems with diverse functionalities.[118–120] For example, by using **G12** as building blocks, Sun prepared **G12**-based microneedle materials.[53] The introduction of vitamin B$_{12}$ into this platform could provide access to diverse
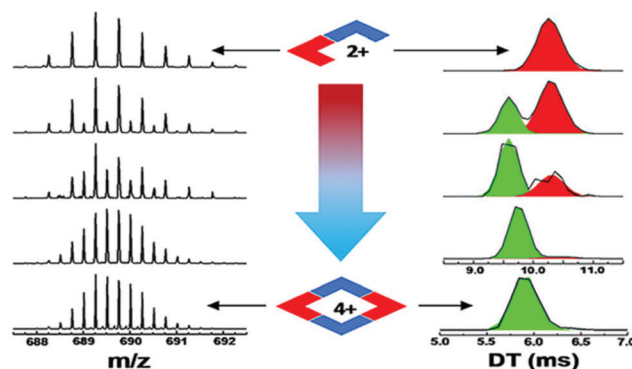

Fig. 6 Gaussian peak-fitting IM spectra resulting from CID of the isobaric nitrate-free rhomboid and half-rhomboid. Figure adapted from ref. 114 with permission from The American Society for Mass Spectrometry, Copyright 2019.
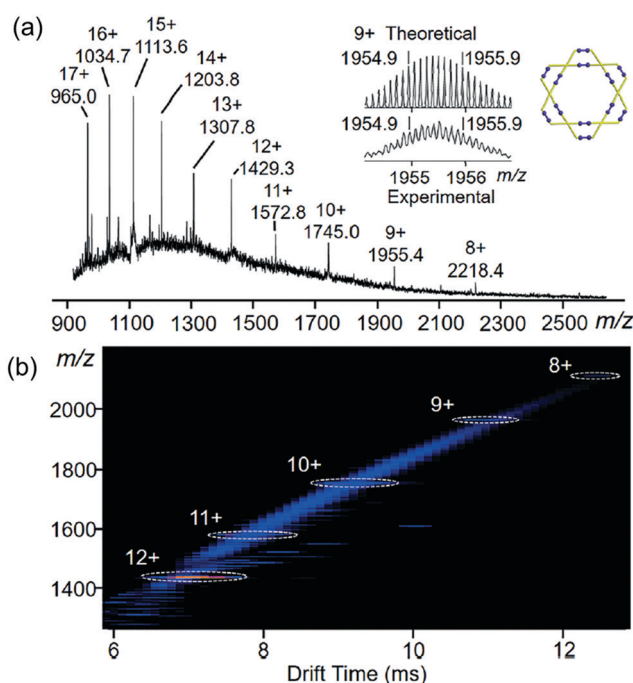

Fig. 7 (a) ESI-MS and (b) IM-MS plot of **M77**. Figure adapted from ref. 93 with permission from Wiley-VCH, Copyright 2017.

artificial biological functions for mimicking natural synthesis systems (Fig. 36).

The hierarchical self-assembly of a rod-like TMV (tobacco mosaic virus) with **M66** resulted in the formation of fibers.[88] Due to the confinement effect in the resultant architectures, the AIE properties caused a notable enhancement in fluorescence (Fig. 37).

By using a coordination cage (**G50**) as the node, a supramolecular coordination framework (SCF) was prepared.[61] This material exhibits an adamantanoid-to-adamantanoid substructure with two sets of cavities, namely, the interior cavity of the adamantanoid cage and the exterior adamantanoid space between **G50** in the network (Fig. 38).
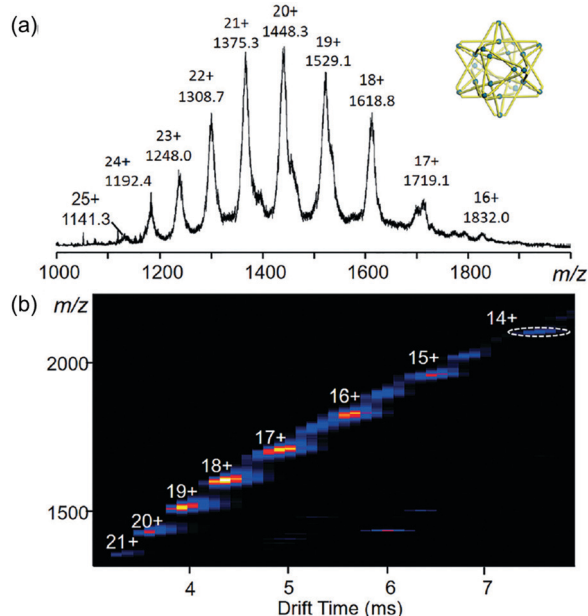
Fig. 8 (a) ESI-MS and (b) IM-MS plot of **M48**. Figure adapted from ref. 93 with permission from Wiley-VCH, Copyright 2017.
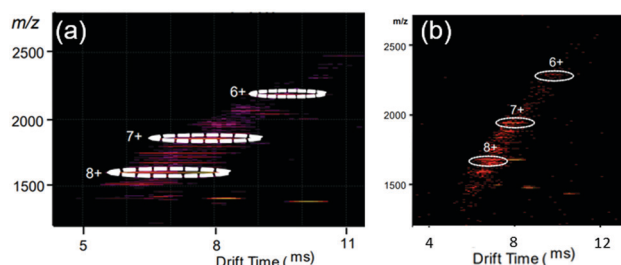

Fig. 11 Photographs of **G13–16** in different solvents. Figure adapted from ref. 54 with permission from American Chemical Society, Copyright 2018.

Fig. 9 ESI-MS and IM-MS plots of **G38/39**. Figure adapted from ref. 107 with permission from American Chemical Society, Copyright 2019.

Fig. 12 Emission spectra of **M15** and a bis-ammonium linker at different concentrations; (inset) photograph of **M15**, bis-ammonium linker, and their mixture upon excitation (λ_{ex} = 365 nm). Figure adapted from ref. 41 with permission from the National Academy of Sciences, Copyright 2017.
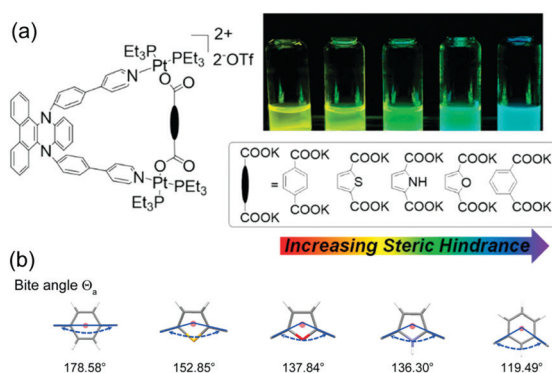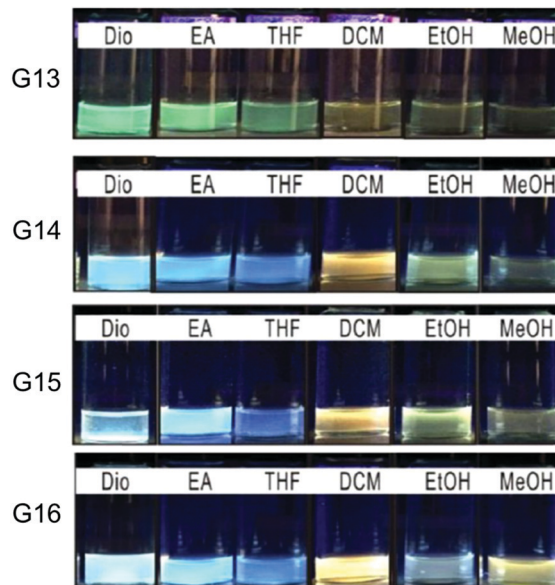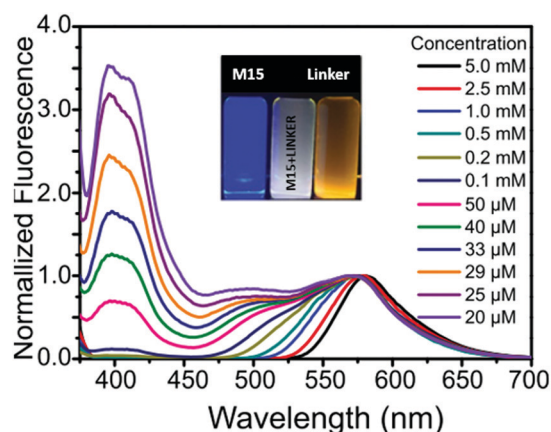

Fig. 10 (a) Self-assembly of **M104–108**, controlled by increasing steric hindrance from **M104–108**. (b) Ground-state structures of titled molecules. Figure adapted from ref. 46 with permission from American Chemical Society, Copyright 2019.
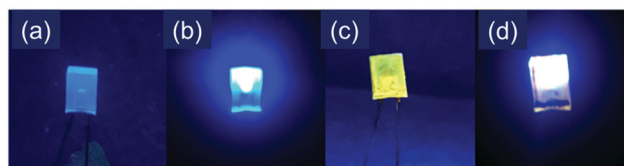

Fig. 13 (a) LED off, (b) LED on, (c) lamp painted with **M25** and bis-ammonium salt (LED off), and (d) lamp painted with **M25** and bis-ammonium salt (LED on). Figure adapted from ref. 37 with permission from American Chemical Society, Copyright 2018.

Datta combined CDSA with host–guest interactions to form various suprastructures, including nanospheres and tapes, depending upon the concentration.[80] In these suprastructures,

CDSA provides the first level of assembly, while host–guest interactions and hydrogen bonding drive the second level of organization (Fig. 39).

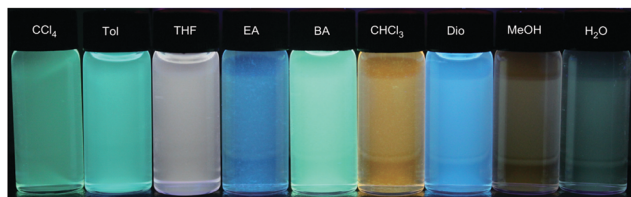This journal is © The Royal Society of Chemistry 2020

Chem. Soc. Rev., 2020, **49**, 3889–3919 | **3905**

Fig. 14   **G18** in different solvents. Figure adapted from ref. 56 with permission from Springer Nature, Copyright 2015.

Fig. 17   Metallacycles **M66–68** and metallacage **G21–23** in CH_2Cl_2. Figure adapted from ref. 87 with permission from American Chemical Society, Copyright 2016.
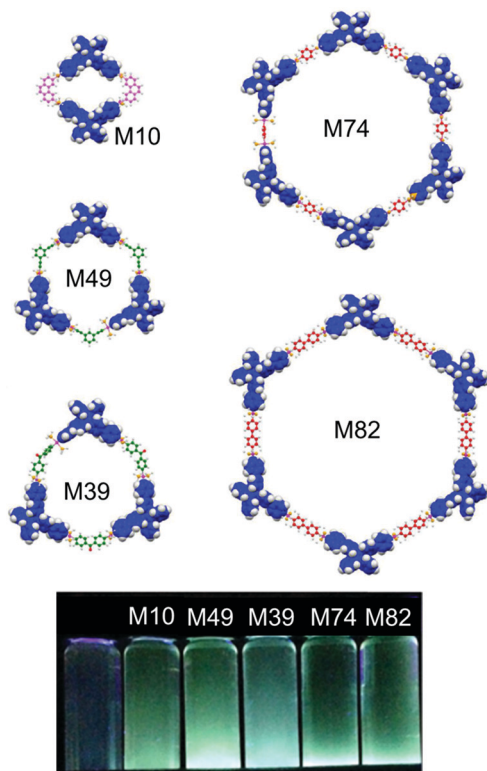

Fig. 15   **M10**, **49**, **39**, **74**, and **82** in CH_2Cl_2. Figure adapted from ref. 65 with permission from American Chemical Society, Copyright 2015.
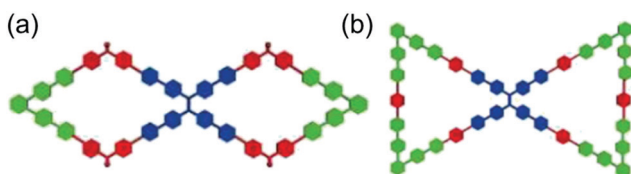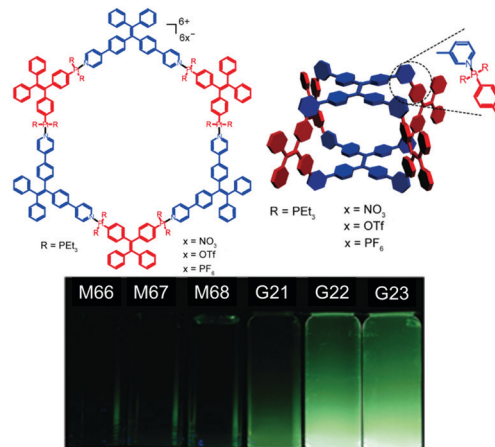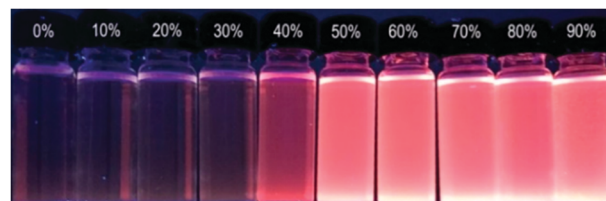

Fig. 18   Photographs of **G11** in CH_2Cl_2/hexane mixtures with different fractions of hexane upon excitation at 365 nm using a UV lamp. Figure adapted from ref. 51 with permission from American Chemical Society, Copyright 2019.
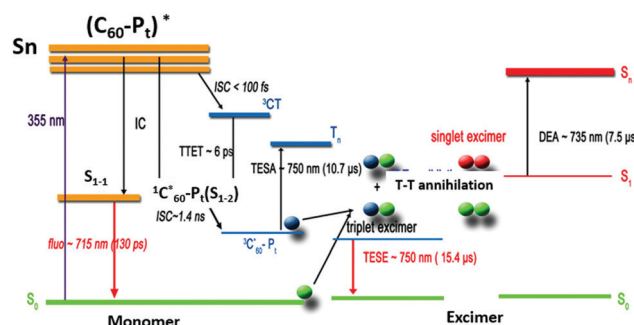

Fig. 16   Scheme of (a) **M43** and (b) **M78**. Figure adapted from ref. 70 with permission from National Academy of Sciences, Copyright 2019.

Fig. 19   Excited-state decay pathways of C_{60}–Pt complexes. Figure adapted from ref. 115 with permission from American Chemical Society, Copyright 2017.

Stang prepared Janus metallacycle **M9**.[47] In an aqueous solution, the hierarchical self-assembly of the supramolecular system was induced by a combination of CDSA and hydrophobic interactions, resulting in the formation of micrometre fibres (Fig. 40).

Triggered by visible light, stable triphenylamine (TPA) radical cations of **M3** could be generated in both the solution and solid states.[36] Furthermore, **M3** was able to hierarchically self-assemble

into nanovesicles in solution (Fig. 41); nanospheres can be formed in the solid phase mainly due to TPA radical interactions and aromatic stacking interactions. Sun used **G13–16** as building blocks for hierarchical assembly.[54] Depending on the substituents and solvents, diverse suprastructures (microwires, plates, and spheres) with tuneable emissions were prepared (Fig. 42).

Sun described the preparation of alanine-based chiral metallacycles **M31/51**.[67] They assembled into nanospheres at low concentrations and generated chiral metallogels at high concentrations (Fig. 43). The molecular chirality of the metallacycles
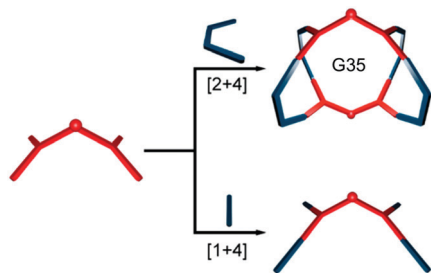
3906 | *Chem. Soc. Rev.*, 2020, **49**, 3889–3919

This journal is © The Royal Society of Chemistry 2020

Fig. 20 Scheme showing (top) **G35** and (bottom) the acyclic assembly. Figure adapted from ref. 105 with permission from American Chemical Society, Copyright 2019.
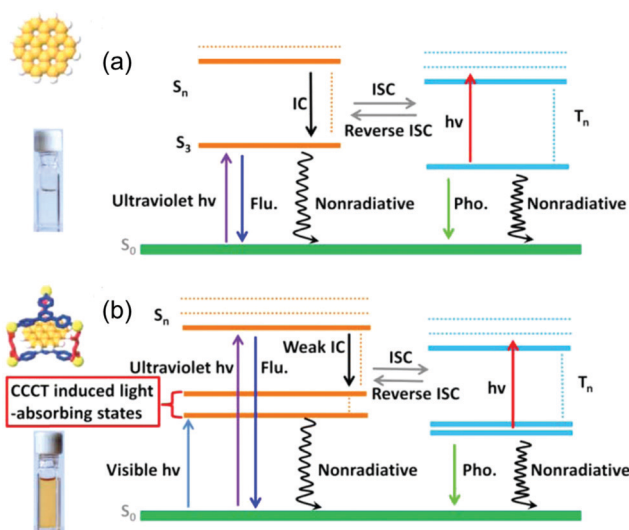

Fig. 21 CCCT-induced light-absorbing states and mechanisms of the various excited-state decay pathways for (a) the coronene and (b) the cage–coronene system. Figure adapted from ref. 50 with permission from American Chemical Society, Copyright 2015.
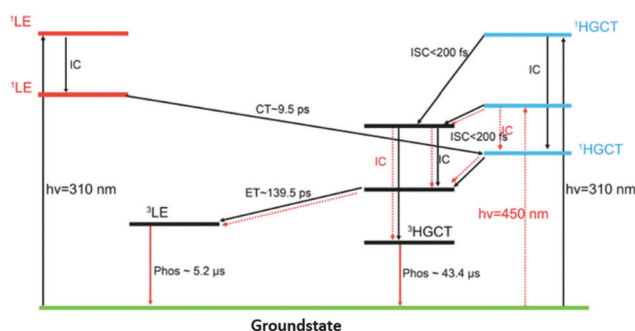

Fig. 22 Primary excited-state decay pathways in the host/guest cage **G1**. Figure adapted from ref. 99 with permission from Royal Society of Chemistry, Copyright 2018.

Fig. 23 Schematic of the reorganization between **M91/G3** and divalent metal ions. Figure adapted from ref. 94 with permission from the Royal Society of Chemistry, Copyright 2017.

Fig. 24 Representation of the formation of a host–guest complex by (a) stepwise and (b) one-pot self-assembly. Figure adapted from ref. 49 with permission from American Chemical Society, Copyright 2017.

Fig. 25 Schematic representation of the host–guest complexation between **G28** and pyrene. Figure adapted from ref. 52 with permission from Wiley-VCH, Copyright 2016.
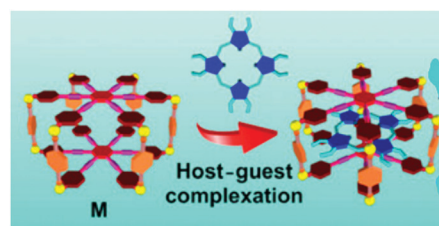
Fig. 26 Cartoon illustration of the preparation of **G33** and octaethyl-porphine. Figure adapted from ref. 58 with permission from National Academy of Sciences, Copyright 2019.

was transferred to the supramolecular architecture through the metallogelation process.

Cao reported the preparation of **G49/50**-based networks with tetra(4-(4-pyridinyl)phenyl)methane as the node and linear platinum(II) ligands as the linkers.[60]
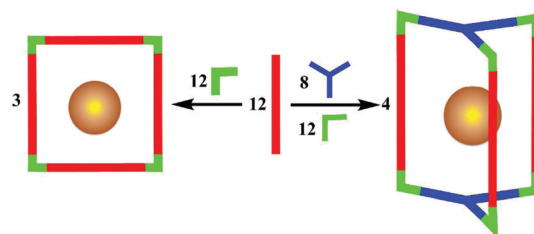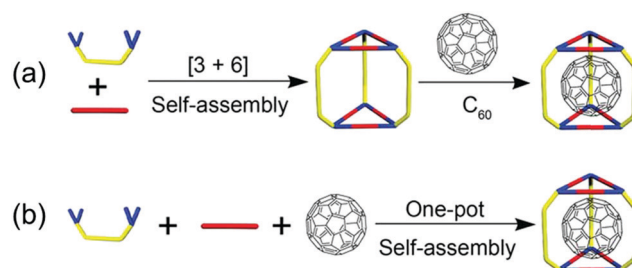
These framework materials possess well-defined periodicity and porosity. These rigid frameworks can be directly converted into a metallogel when prepared in DMSO with the concentration increased (Fig. 44).[60]

As shown in Fig. 45, by combining metal–ligand coordination, hydrogen bonding, and host–guest interactions in a hierarchical fashion, **M62**-based supramolecular polymers were prepared.[84]

This journal is © The Royal Society of Chemistry 2020

Chem. Soc. Rev., 2020, **49**, 3889–3919 | **3907**

Fig. 27 Recognition of D-glucose (a) in a hydrogen-bonding cavity and (b) in a polyaromatic cavity. (c) **G54** and dD its slice through the centre of the crystal structure. Figure adapted from ref. 111 with permission from AAAS, Copyright 2017.

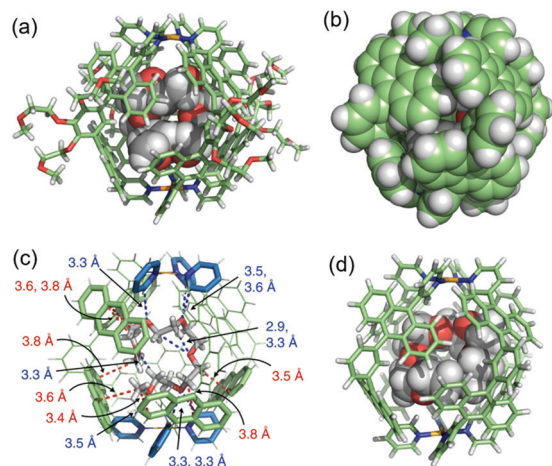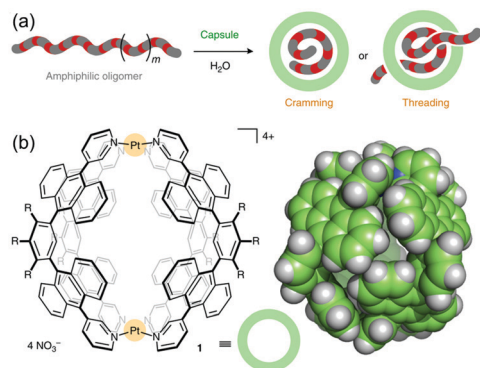Fig. 28 (a) Schematic representation of the cramming or threading of long amphiphilic oligomers into a **G54**. (b) **G54** and the X-ray crystal structure. Figure adapted from ref. 112 with permission from Springer Nature, Copyright 2018.
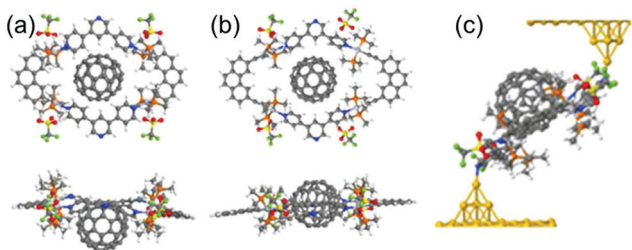

Fig. 29 (a) **M11** + C_{60}; (b) **M30** + C_{60}; (c) [**M11** + C_{60}] where the angles between the Au–N bond. Figure adapted from ref. 64 with permission from Springer Nature, Copyright 2019.

Metallacycles **M80/81** formed a yellow, translucent metallogel in cyclohexane and CH_2Cl_2 (v/v = 2/5) when the concentration was increased to 1.3 μM.[62] It was proposed that the fibrous structures were first formed mainly through intermolecular
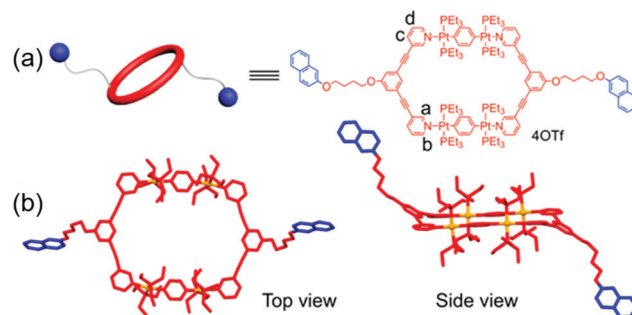

Fig. 30 (a) Cartoon representation and chemical structure of **M70**; (b) top and side views of the single-crystal structure of **M70**. Figure adapted from ref. 90 with permission from American Chemical Society, Copyright 2019.
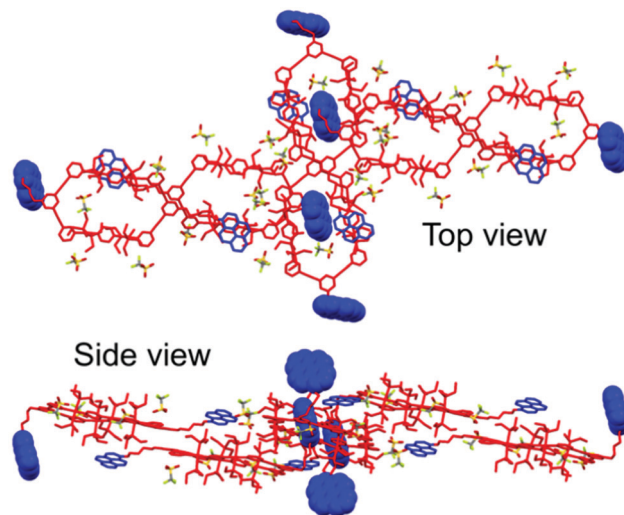

Fig. 31 Assembled single crystal of **M71** produced by the host–guest complexation. Figure adapted from ref. 91 with permission from American Chemical Society, Copyright 2019.

Pt···Pt and π–π stacking interactions. Then, as the concentration was increased, a fibre-based network was formed because of the cross-linking of the fibres, which ultimately generated a stable supramolecular metallogel (Fig. 46).

By using well-defined metallacycles (**M41/54**) as the cores, Yang prepared a family of star supramolecular polymers. In water, the obtained polymer behaved typically for a material with a lower critical solution temperature[72] and formed a supramolecular hydrogel (Fig. 47).

Yin prepared **G24**, dissolved it in acetone, and to that solution was added a solution of a bis-ammonium linker in acetone.[55] A **G24**-based supramolecular gel was formed by mixing these two solutions. Both thermally induced and potassium-ion-induced gel–sol transitions can be observed by the naked eye (Fig. 48).

Host–guest interactions between a bis-ammonium salt and **M26–29** drive the formation of supramolecular polymers.[66] By continuously increasing the concentration of polymer, a gel with self-healing properties was obtained (Fig. 49).

3908 | Chem. Soc. Rev., 2020, 49, 3889–3919

This journal is © The Royal Society of Chemistry 2020
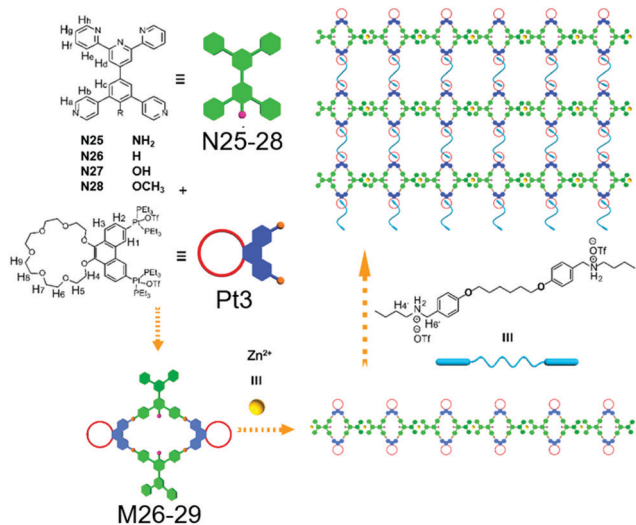
Fig. 32 Supramolecular polymeric network. Figure adapted from ref. 66 with permission from American Chemical Society, Copyright 2019.
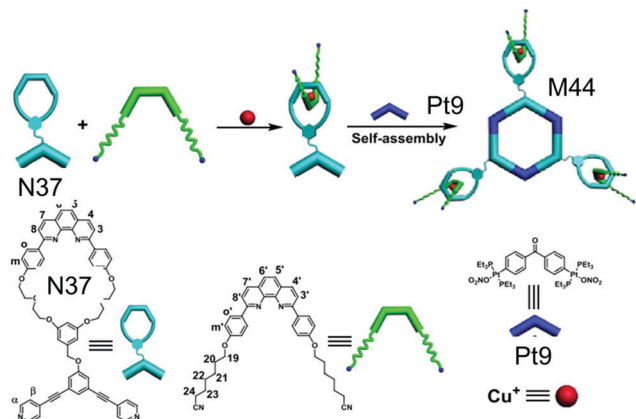
Fig. 33 Self-assembled **M44**. Figure adapted from ref. 74 with permission from American Chemical Society, Copyright 2018.
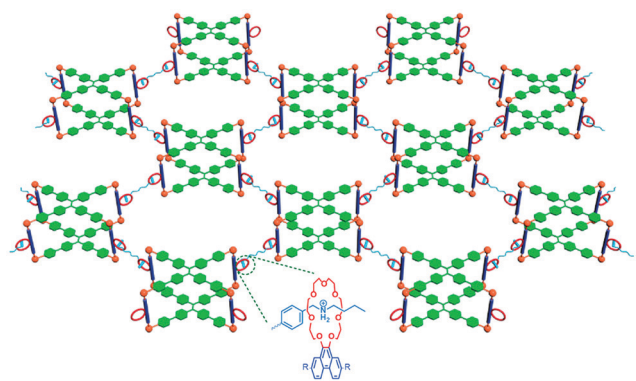
Fig. 34 Formation of a supramolecular polymer network from **G24** and bisammonium salt. Figure adapted from ref. 55 with permission from American Chemical Society, Copyright 2018.
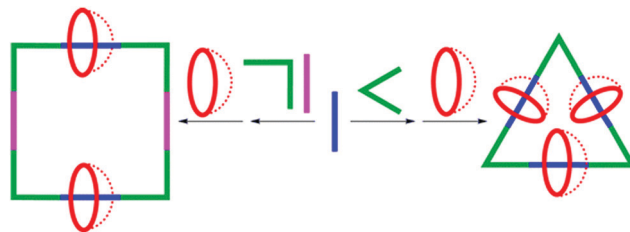
Fig. 35 Self-assembly of supramolecular rectangles and [3]catenanes. Figure adapted from ref. 117 with permission from American Chemical Society, Copyright 2015.

Fig. 36 **G12**-based micrometre needles. Figure adapted from ref. 53 with permission from American Chemical Society, Copyright 2018.
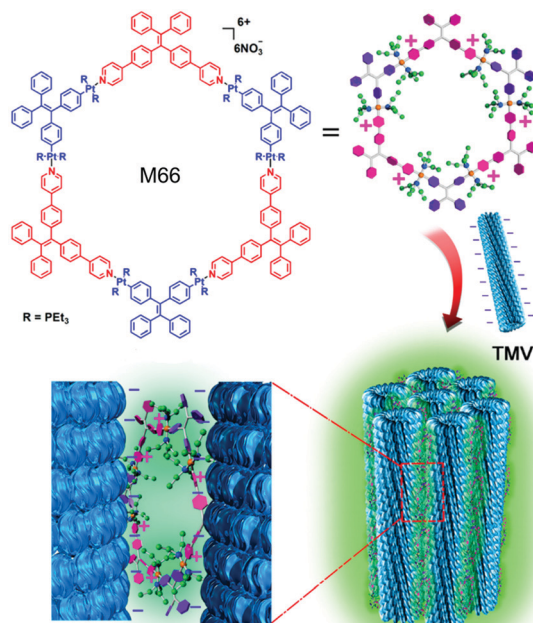
Fig. 37 Coassembly of **M66** with TMV. Figure adapted from ref. 88 with permission from American Chemical Society, Copyright 2016.

This journal is © The Royal Society of Chemistry 2020

Chem. Soc. Rev., 2020, **49**, 3889–3919 | **3909**
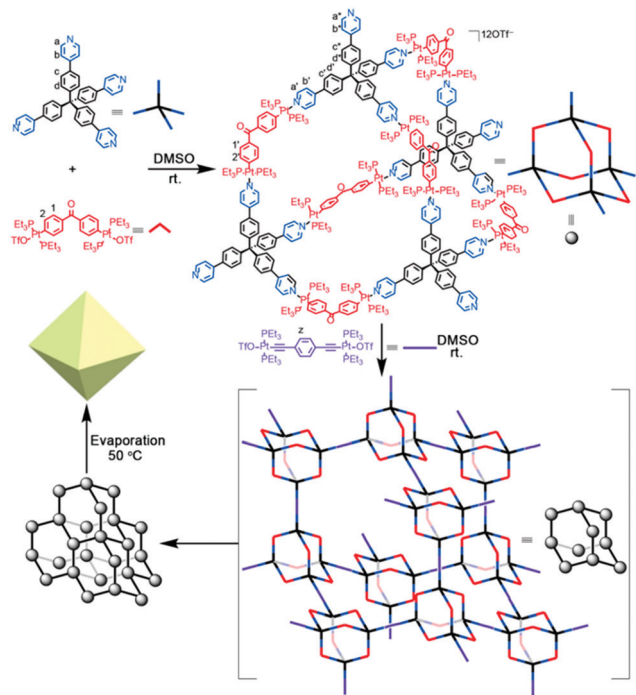
Fig. 38 **G50**-based adamantoid materials. Figure adapted from ref. 61 with permission from American Chemical Society, Copyright 2018.
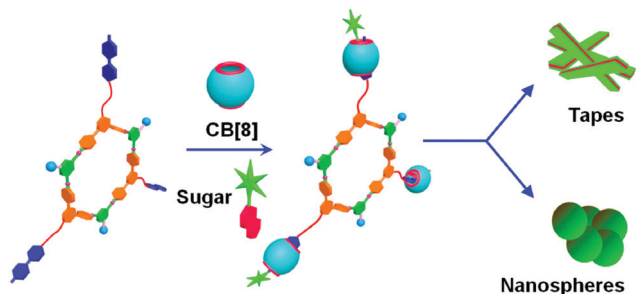
Fig. 39 **M55**-based nanospheres and tapes. Figure adapted from ref. 80 with permission from American Chemical Society, Copyright 2018.
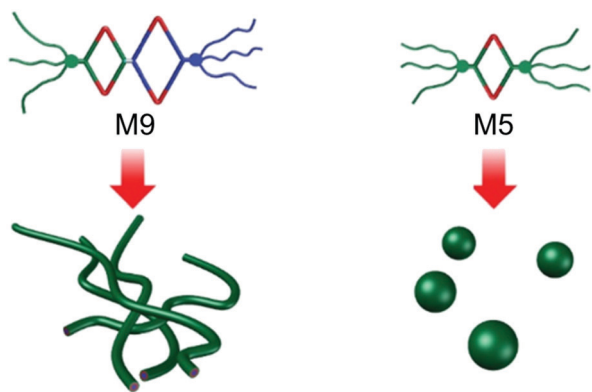
Fig. 40 **M9/5**-based nanospheres and tapes. Figure adapted from ref. 47 with permission from American Chemical Society, Copyright 2019.
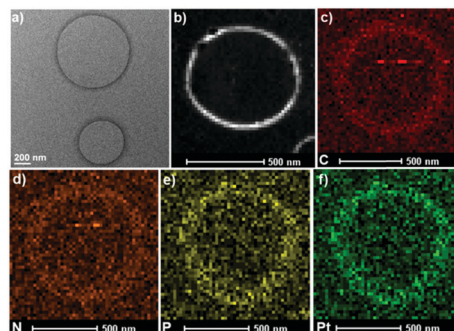
Fig. 41 **M3**-based nanovesicles. Figure adapted from ref. 36 with permission from the American Chemical Society, Copyright 2019.
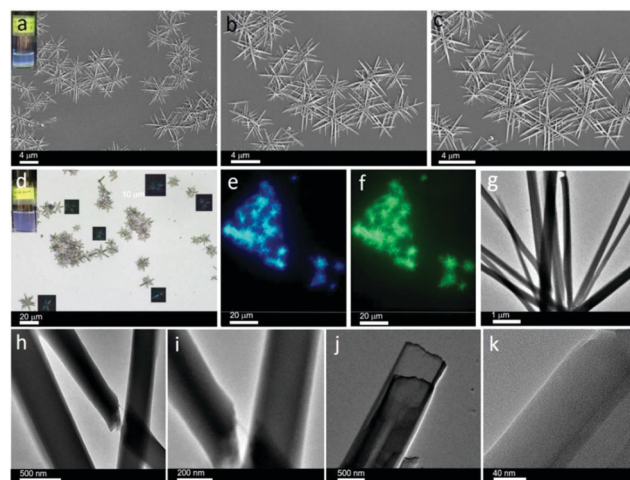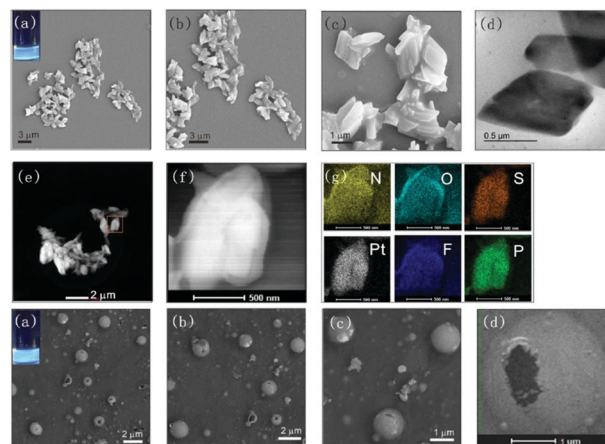

Fig. 42 **G14**-based micrometre-scale plates, and **G15**-based micrometre-scale hollow spheres. Figure adapted from ref. 54 with permission from the American Chemical Society, Copyright 2018.
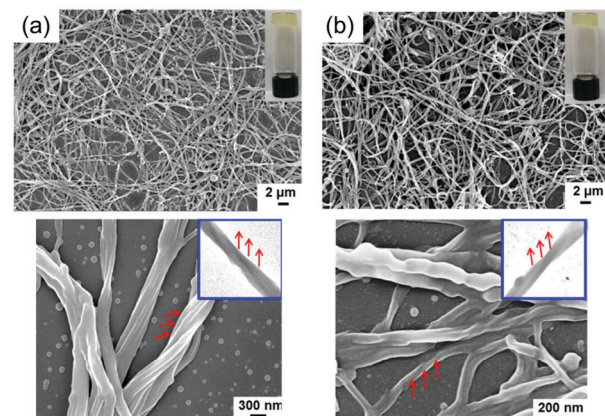
Fig. 43 (a) **M31** (b) **M51**-based metallogels. Figure adapted from ref. 67 with permission from American Chemical Society, Copyright 2017.

4.4 Stimuli-triggered transformations

Stimuli such as solvents, anions, and changes in the component fractions have been extensively employed to trigger transformation processes of MOCs. For example, starting from functionalized metallacycle **M47**,[76] a structural conversion of

3910 | *Chem. Soc. Rev.*, 2020, **49**, 3889–3919

This journal is © The Royal Society of Chemistry 2020
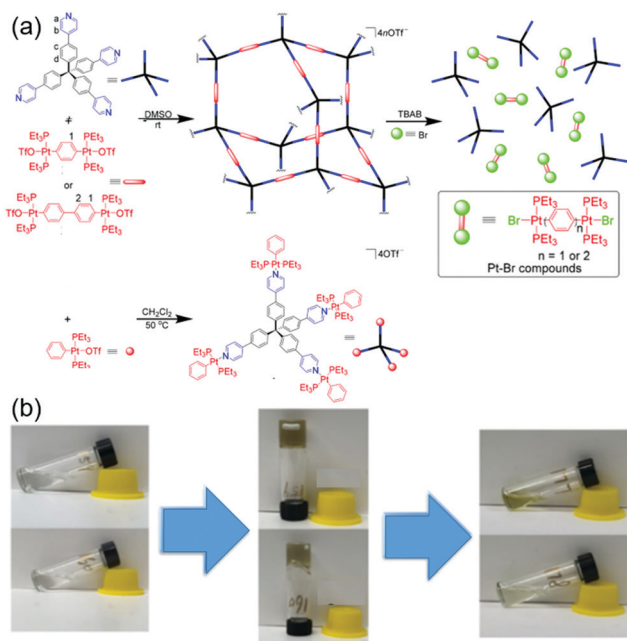
Fig. 44 (a) Synthesis and disassembly of diamondoid frameworks and tetrahedral **G49/50**; (b) photographs of 1 (left) and 3 and 3 + TBAB (right) in DMSO. Figure adapted from ref. 60 with permission from American Chemical Society, Copyright 2019.

Fig. 45 (a) Photograph of the **M62**-based metallogel. (b) SEM image of the xerogel of **M62**. Figure adapted from ref. 84 with permission from American Chemical Society, Copyright 2016.

Fig. 46 Proposed process for the formation of a supramolecular metal-logel and the guest-induced gel-to-sol transformation. Figure adapted from ref. 62 with permission from Wiley-VCH, Copyright 2016.

Fig. 47 (a) The mechanism of self-healing of a supramolecular polymeric hydrogel. (b) Photographs of the self-healing experiments. Figure adapted from ref. 72 with permission from American Chemical Society, Copyright 2016.
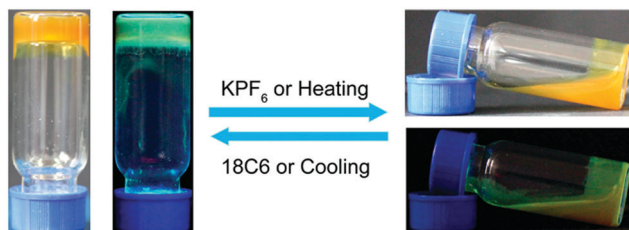
Fig. 48 Optical and fluorescence photographs of the gel–sol transition of gel. Figure adapted from ref. 55 with permission from American Chemical Society, Copyright 2018.

the transplatinum acetylide moiety can be triggered by simple phosphine ligand-exchange reactions (Fig. 50).[76]

In response to solvent composition, negative solvatochromic emission (NSE) from a conformational change in a coordination cage was demonstrated by Liu. When the solvent was changed from acetone/acetonitrile/methanol to water, the emission of **G12** gradually shifts to a shorter wavelength.[101] Intramolecular π–π stacking and hydrophobic interactions between the TPPE planes drive molecular conformational change during this process (Fig. 51).

5. Applications

Stimuli-responsive elements can be incorporated into MOCs using conventional techniques, resulting in profound implications for the development of smart materials,[15] biomedicines,[29,30] catalysis,[121] and so on.
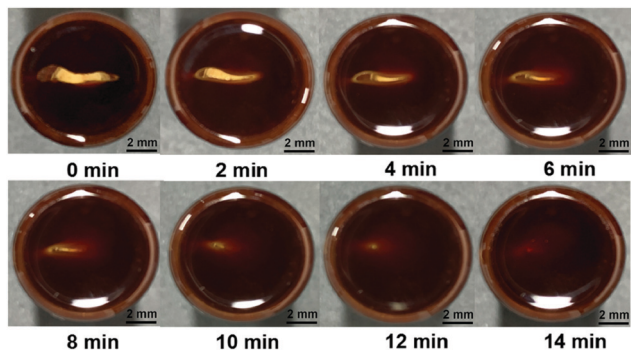
Fig. 49 Photographs of the self-healing process. Figure adapted from ref. 66 with permission from American Chemical Society, Copyright 2019.
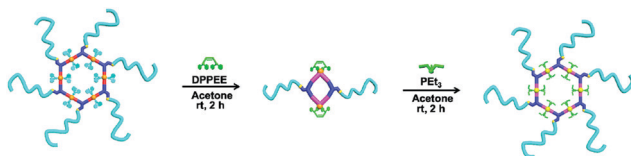
Fig. 50 Graphical representation of the synthesis of metallacycle and a metallacycle-linked star polymer. Figure adapted from ref. 76 with permission from American Chemical Society, Copyright 2019.
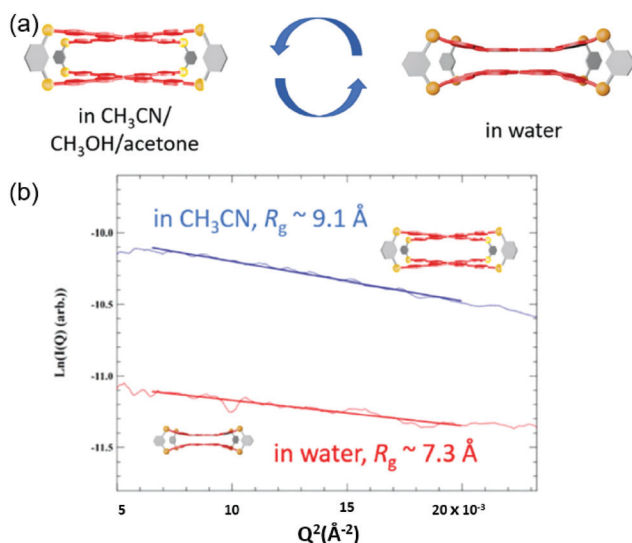
Fig. 51 (a) Illustration of the proposed conformational change of **G12** in different solvents. (b) Guinier analysis of **G12** in aqueous (red) and acetonitrile solutions (blue). Figure adapted from ref. 101 with permission from Royal Society of Chemistry, Copyright 2019.

5.1 MOC-based environmentally responsive materials

Hexagonal metallacycles **M50** and **M85**, with three and six anthracene groups, respectively, were synthesized by Tang.[77] Both **M50** and **M85** showed reversible changes in their absorption and emission spectra between −20 and 60 °C (Fig. 52).

Chirality-tuneable metallacycles **M64/65**[86] containing two light-responsive units and two chiral naphthol units were constructed by CDSA. Upon irradiation with ultraviolet and
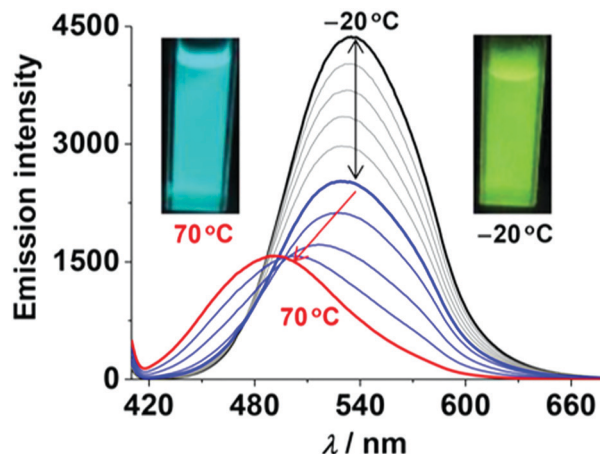
Fig. 52 Emission spectral changes (**M50**). Figure adapted from ref. 77 with permission from American Chemical Society, Copyright 2018.
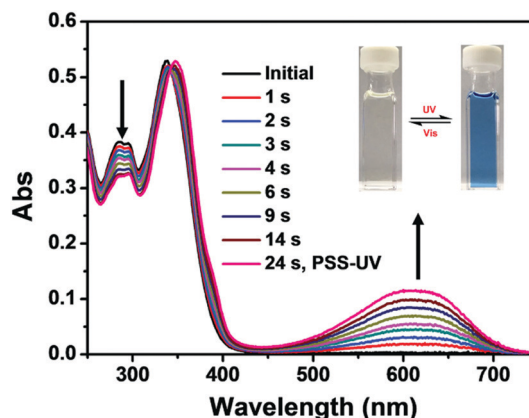
Fig. 53 Absorption spectral changes of **M65** upon UV (365 nm) irradiation. Figure adapted from ref. 86 with permission from Wiley-VCH, Copyright 2018.

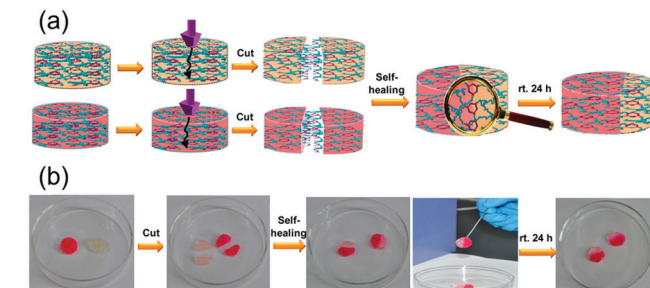visible light, the conformations of these metallacycles underwent reversible transformations between ring-open and ring-closed forms, as demonstrated by an obvious change in their CD curves (Fig. 53).[86]

The **M80**-based vapochromic system features not only high selectivity for CH_2Cl_2 vapor molecules but also ultrastability.[92] At room temperature, when exposed to CH_2Cl_2 vapour, **M80** displayed a colour change from yellow to red. Furthermore, following exposure to CH_2Cl_2 vapour, **M80** retained its red colour in air for several months (Fig. 54).

M59 and **M92** have been used to detect nitroaromatic explosives.[82] Based on fluorescence quenching, thin films of highly luminescent **M59** and **M92** showed efficient sensing of nitroaromatic compounds in the vapour phase (Fig. 55).

In the substrate-supported state, the quantum yield (QY) of **M100** exceeded that of **N59**, which can be used for sensing.[44] Because the metallacycle prevents the dense packing of the compound, the maximum emission of the **M100**-based film appears at 620 nm, but that of the **N59**-based film appears at 570 nm (Fig. 56).[44]

3912 | *Chem. Soc. Rev.*, 2020, **49**, 3889–3919

This journal is © The Royal Society of Chemistry 2020

Fig. 54 Photographs showing the dynamic colour changes under ambient light for the reversible vapochromic phenomenon of **M80/81**. Figure adapted from ref. 92 with permission from American Chemical Society, Copyright 2016.
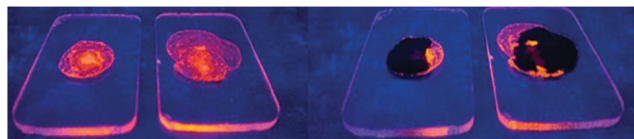
Fig. 55 Fluorescence images of thin films of compounds **M59** and **M92** after exposure to NB (nitrobenzene). Figure adapted from ref. 82 with permission from Wiley-VCH, Copyright 2016.
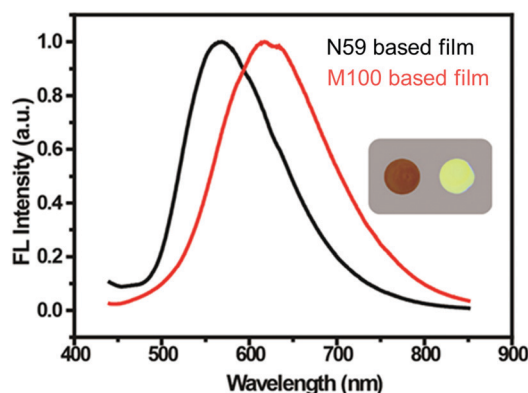
Fig. 56 Fluorescence spectra of **M100** and **N59**-based silica gel plate-supported films. Figure adapted from ref. 44 with permission from American Chemical Society, Copyright 2019.

Fig. 57 The emission intensities of **G26** at 500 nm as a function of cysteine. Figure adapted from ref. 57 with permission from American Chemical Society, Copyright 2017.
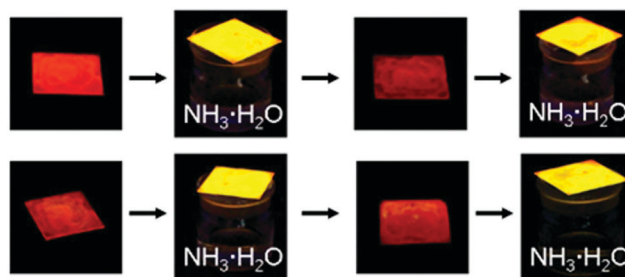
Fig. 58 Photographs of films of **M102** when exposed to or removed from ammonia under a UV lamp at 365 nm. Figure adapted from ref. 96 with permission from American Chemical Society, Copyright 2017.
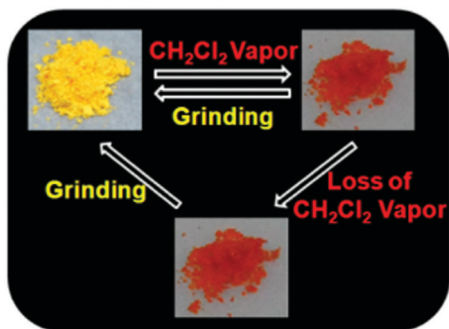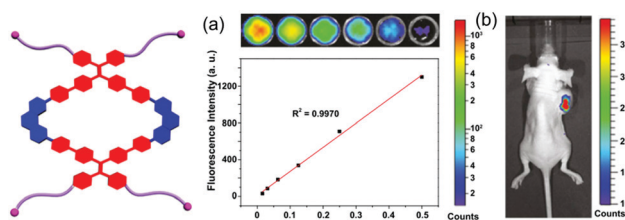

Fig. 59 (left) Schematic representation of **M14**. (a) Plot and fitting of the fluorescence intensity of **M14** *versus* their concentration. (b) A treated with **M14**. Figure adapted from ref. 38 with permission from National Academy of Sciences, Copyright 2016.

Zhang prepared three different tetragonal metallacages, **G25–27**.[57] A self-destructive mechanism of **G26** caused by thiol-containing amino acid was demonstrated in methanol/water (Fig. 57).

M102 and **M103** films were used as ammonia sensors as they changed colour from red to yellow upon exposure to ammonia and returned to their initial colour upon removal of the ammonia.[96] When the **M102** film was exposed to ammonia vapor, an obvious colour change from red to yellow was observed (Fig. 58).

5.2 Biomedical applications

5.2.1 Metallacycles.
TPE-containing fluorescent rhomboid **M14** was used in cell imaging, and it showed significant enrichment in lung cells (Fig. 59).[38]

Sun designed and synthesized a NIR-II theranostic nanoprobe involving **M34**, which has a long emission wavelength.[40] This design gives the nanoprobe good photostability and passive targeting ability, and therefore, it can facilitate the precise diagnosis of cancer with high resolution and selective delivery of **M34** to the tumour region. Compared with probes in previous reports, this nanoprobe shows enhanced permeability and retention effects. *In vitro* and *in vivo* results further indicated that the nanoprobe has higher antitumour efficacy and fewer side effects than cisplatin. As shown in Fig. 60, the fluorescence signal at the tumour region was clearly observed even after 2 weeks.

This journal is © The Royal Society of Chemistry 2020

Chem. Soc. Rev., 2020, **49**, 3889–3919 | **3913**

Fig. 60 NIR-II images of monitoring the **M34** therapeutic response in HepG2 tumours. Figure adapted from ref. 40 with permission from National Academy of Sciences, Copyright 2019.
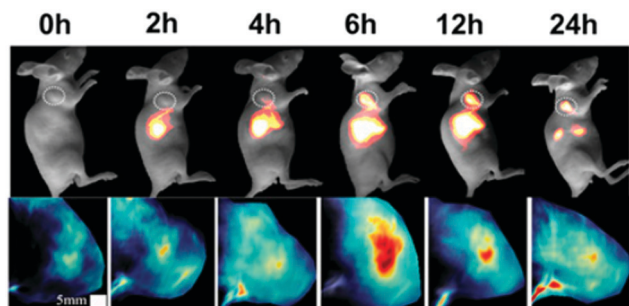
Fig. 61 NIR-II fluorescence and PA (photoacoustic) images of U87MG tumour mice at different times after tail vein injection of **M35**. Figure adapted from ref. 39 with permission from National Academy of Sciences, Copyright 2019.

Sun engineered a dual-modal imaging and chemophotothermal therapeutic nanoagent that incorporates **M35** and a fluorescent dye into multifunctional melanin dots that have photoacoustic and photothermal features.[39] A combination of the antitumour activity of **M35** and the inherent photothermal properties of melanin dots synergistically enabled chemophotothermal therapy to be precisely performed and gave the desired treatment effects with fewer side effects and increased lifetimes (Fig. 61).[39]

5.2.2 Metallacages. Terenzi and co-workers prepared three quadrangular boxes, **G43–45** (Fig. 62), of distinct size that showed biological activity against cancer cells by influencing the expression of genes known to form guanine quadruplexes.[108]

Sleiman obtained platinum squares (**M87–90**) and examined their binding to DNA and RNA guanine quadruplexes (Fig. 63).[43] **M87–90** showed submicromolar binding affinities for the RNA telomeric sequence, which regulates telomere elongation in both telomerase-positive/negative cancer cells.
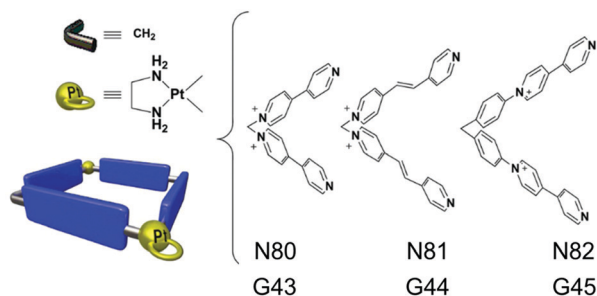
Fig. 62 Schematic representation of **G43–45**. Figure adapted from ref. 108 with permission from Royal Society of Chemistry, Copyright 2017.
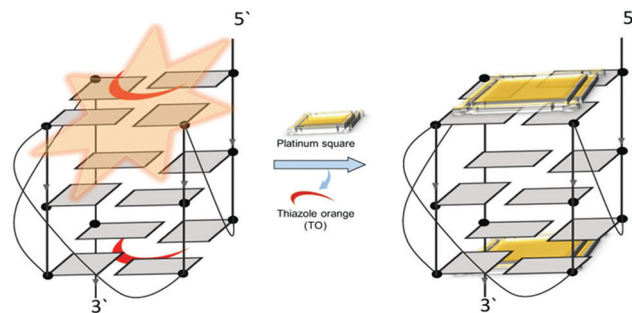
Fig. 63 Schematic of the competitive fluorescence displacement assay. Figure adapted from ref. 43 with permission from American Chemical Society, Copyright 2017.
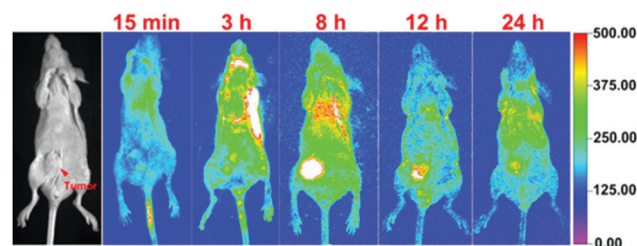
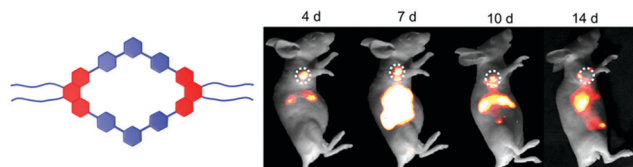**Fig. 64** Fluorescence imaging of nude mice with HeLa cancer xenografts after treatment. Figure adapted from ref. 103 with permission from National Academy of Sciences, Copyright 2016.

Chen used metallacage **G19** to construct theranostic supramolecular nanoparticles.[103] The fluorescence of localized MNPs in tumour tissues gradually increased with time (Fig. 64).

Yu prepared porphyrin-based metallacages, **G28–30**, and then used these cages for the fabrication of MNPs and studied their antitumour activity.[104] By combining NIRFI, PET, and MRI, they achieved precise detection as well as therapy for some tumours. The combination of chemotherapy and PDT (photodynamic therapy) effectively ablated A2780CIS cells in mice without recurrence during the course of therapy. Combination of PDT (eliminated the primary tumour) and the chemotherapeutic drug (killed the residual cancer cells), inhibiting tumour recurrence (Fig. 65).

Yu prepared platinum-based anticancer drug **G33** and loaded it as a cargo to encapsulate a photosensitizer.[58] The resulting assemblies could co-deliver chemotherapeutic agents and photosensitizers. The as-prepared MNPs could specifically deliver **Pt7** and a photosensitizer to cancer cells. The MNPs accumulated at tumour sites. By combining chemotherapy and PDT, *in vivo* studies in a drug-resistant tumour model demonstrated that MNPs exhibited superior antitumour activity (Fig. 66).[58]

Zhou described the use of molecular self-assembly for accessing **G52** with strong 2-photon absorption by combining multiple Ru(II) complexes with Pt(II) building blocks *via* coordination.[79] **G52** was encapsulated in a polymer to form nanoparticles that, upon internalization into cells, accumulate in the lysosomes, leading to high photocytotoxicity. The effect of 2-photon PDT on tumour growth was assessed by monitoring

3914 | *Chem. Soc. Rev.*, 2020, **49**, 3889–3919

This journal is © The Royal Society of Chemistry 2020
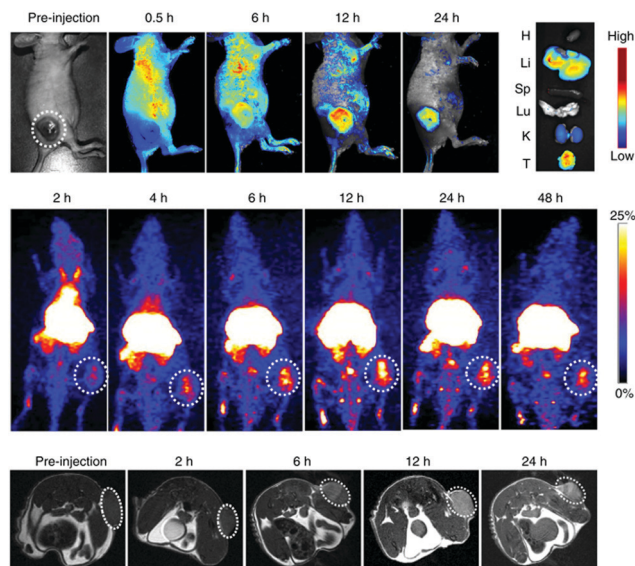
Fig. 65 Mice before and after treatment. Figure adapted from ref. 104 with permission from Springer Nature, Copyright 2018.
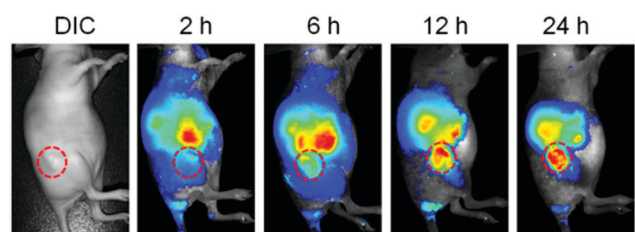
Fig. 66 Time-dependent fluorescence images of A2780CIS tumour-bearing mice after *in vivo* injection of **G33**-loaded MNPs. Figure adapted from ref. 58 with permission from National Academy of Sciences, Copyright 2019.

the tumour volumes in the mice over a period of 15 days (Fig. 67).

5.2.3   Antibacterial activity. M66 acts as a photosensitizer with aggregation-induced emission.[87] It self-assembles with a transacting activator of transduction peptide-decorated virus coat protein through electrostatic interactions. This assembly exhibits both ROS generation and a strong membrane-intercalating
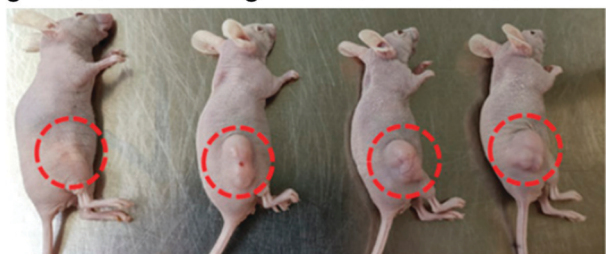
Fig. 67 Representative photographs of A549 tumours in mice with different treatments. Figure adapted from ref. 79 with permission from National Academy of Sciences, Copyright 2019.
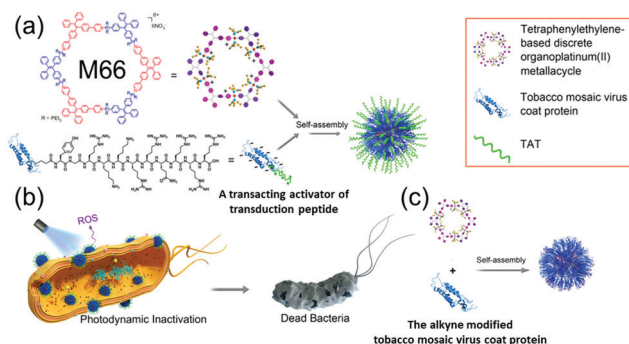
Fig. 68 Schematic illustration of the self-assembly of (a) **M66** and a transacting activator of transduction peptide. (b) Antibacterial mechanism. (c) **M66** and protein the alkyne-modified tobacco mosaic virus coat protein. Figure adapted from ref. 122 with permission from National Academy of Sciences, Copyright 2019.

abilities, resulting in significantly enhanced PDI (photodynamic inactivation) efficiency against bacteria (Fig. 68).[122]

5.3   Catalysis activity

MOCs have attracted particular interest due to their structural modifiability and tuneable chemical properties, which are quite important in catalysis.[123] Recently, Fe-,[124] Co-,[125,126] Zn-,[127] and Rh[128]-based tetrahedral cages and cubes have been used as catalysts. For example, Hooley and co-workers synthesized an Fe_4L_6 cage, which can serve as an effective supramolecular catalyst, providing up to a 1000-fold rate enhancement in acetal solvolysis.[124] MOCs with defined cavities can catalyse chemical reactions with unprecedented selectivity under ambient conditions. Here, Pt(II)-based chiral tetrahedral **G4** features an internal nanocavity,[100] enabling it to catalyse Michael addition reactions of a series of nitrostyrene derivatives with an indole in a water/methanol mixture (Fig. 69). A series of reactions with various nitrostyrene derivatives and indoles in a water/methanol (9/1) mixture were investigated at room temperature.[100]

Yang presented the fabrication of **M42** in the confined cavities of mesoporous carbon FDU-16.[73] To demonstrate that the stability and activity of **M42** can be enhanced in the confined cavity, the catalytic performance was evaluated (Fig. 70). Under the same reaction conditions, **M42** and the
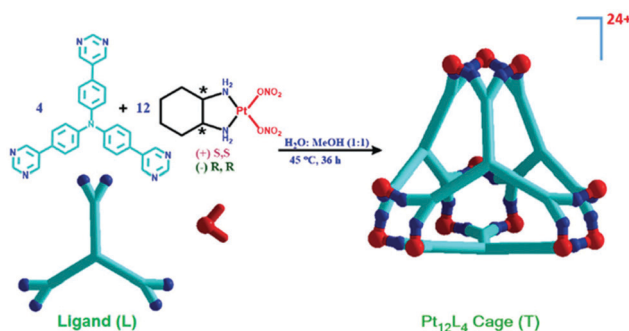
Fig. 69 Schematic of the synthesis of tetrahedral **G4**. Figure adapted from ref. 100 with permission from the Royal Society of Chemistry, Copyright 2018.

This journal is © The Royal Society of Chemistry 2020

Chem. Soc. Rev., 2020, **49**, 3889–3919 | **3915**
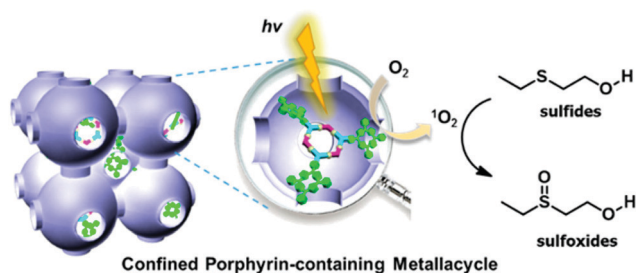
Fig. 70 Scheme for the photooxidation of sulfides. Figure adapted from ref. 73 with permission from American Chemical Society, Copyright 2018.

composites exhibited 42% and 54% conversions, respectively, after 4 h (Fig. 70).[73]

6. Conclusions

A large number of well-defined platinum organometallic species, ranging from metallacycles to metallacages, have been constructed *via* directional bonding, panelling, and dimetallic building block approaches. The applications of these structures for tuning emissions, host–guest interactions, sensing, biomedical and catalysis have been explored. The examples described in this review demonstrate that, through rational chemical manipulations, two-dimensional metallacycles and three-dimensional metallacages that can potentially serve as multifunctional systems, from sensing to catalysis, could be realized. Pt-Containing metallacycles and metallacages will continue to be an active area of research and an important part of materials science. In the future, research in this area will likely be directed towards the formation and characterization of more complicated suprastructures and the exploitation of the functions of platinum metallacycles and metallacages in fields such as sensing, optics, catalysis and biomedical materials.

Conflicts of interest

There are no conflicts to declare.

Acknowledgements

Notes and references

1 G. Vantomme and E. W. Meijer, *Science*, 2019, **363**, 1396–1397.
2 F. Praetorius, B. Kick, K. L. Behler, M. N. Honemann, D. Weuster-Botz and H. Dietz, *Nature*, 2017, **552**, 84.
3 K. Tao, P. Makam, R. Aizen and E. Gazit, *Science*, 2017, **358**, eaam9756.
4 A. J. Simon, Y. Zhou, V. Ramasubramani, J. Glaser, A. Pothukuchy, J. Gollihar, J. C. Gerberich, J. C. Leggere, B. R. Morrow, C. Jung, S. C. Glotzer, D. W. Taylor and A. D. Ellington, *Nat. Chem.*, 2019, **11**, 204–212.
5 J. Rittle, M. J. Field, M. T. Green and F. A. Tezcan, *Nat. Chem.*, 2019, **11**, 434–441.
6 Y. Sun, F. Guo, T. Zuo, J. Hua and G. Diao, *Nat. Commun.*, 2016, **7**, 12042.
7 D. Fujita, Y. Ueda, S. Sato, N. Mizuno, T. Kumasaka and M. Fujita, *Nature*, 2016, **540**, 563–566.
8 P. Ballester, M. Fujita and J. Rebek, *Chem. Soc. Rev.*, 2015, **44**, 392–393.
9 T. R. Cook and P. J. Stang, *Chem. Rev.*, 2015, **115**, 7001–7045.
10 R. Chakrabarty, P. S. Mukherjee and P. J. Stang, *Chem. Rev.*, 2011, **111**, 6810–6918.
11 T. R. Cook, Y.-R. Zheng and P. J. Stang, *Chem. Rev.*, 2013, **113**, 734–777.
12 D. L. Caulder and K. N. Raymond, *Acc. Chem. Res.*, 1999, **32**, 975–982.
13 A. M. Lifschitz, M. S. Rosen, C. M. McGuirk and C. A. Mirkin, *J. Am. Chem. Soc.*, 2015, **137**, 7252–7261.
14 S. Chakraborty and G. R. Newkome, *Chem. Soc. Rev.*, 2018, **47**, 3991–4016.
15 A. J. McConnell, C. S. Wood, P. P. Neelakandan and J. R. Nitschke, *Chem. Rev.*, 2015, **115**, 7729–7793.
16 S. Zarra, D. M. Wood, D. A. Roberts and J. R. Nitschke, *Chem. Soc. Rev.*, 2015, **44**, 419–432.
17 D. Zhang, T. K. Ronson and J. R. Nitschke, *Acc. Chem. Res.*, 2018, **51**, 2423–2436.
18 T. Sawada, A. Saito, K. Tamiya, K. Shimokawa, Y. Hisada and M. Fujita, *Nat. Commun.*, 2019, **10**, 921.
19 G. H. Clever and P. Punt, *Acc. Chem. Res.*, 2017, **50**, 2233–2243.
20 Z. Gao, Y. Han, Z. Gao and F. Wang, *Acc. Chem. Res.*, 2018, **51**, 2719–2729.
21 P. Stricklen and J. Verkade, *J. Am. Chem. Soc.*, 1983, **105**, 2494–2495.
22 Y.-Y. Zhang, W.-X. Gao, L. Lin and G.-X. Jin, *Coord. Chem. Rev.*, 2017, **344**, 323–344.
23 W. M. Bloch and G. H. Clever, *Chem. Commun.*, 2017, **53**, 8506–8516.
24 P. J. Stang and B. Olenyuk, *Acc. Chem. Res.*, 1997, **30**, 502–518.
25 M. Fujita, M. Tominaga, A. Hori and B. Therrien, *Acc. Chem. Res.*, 2005, **38**, 369–378.
26 C. G. Oliveri, P. A. Ulmann, M. J. Wiester and C. A. Mirkin, *Acc. Chem. Res.*, 2008, **41**, 1618–1629.
27 M. D. Ward, C. A. Hunter and N. H. Williams, *Acc. Chem. Res.*, 2018, **51**, 2073–2082.
28 L.-J. Chen and H.-B. Yang, *Acc. Chem. Res.*, 2018, **51**, 2699–2710.
29 H. Sepehrpour, W. Fu, Y. Sun and P. J. Stang, *J. Am. Chem. Soc.*, 2019, **141**, 14005–14020.
30 N. Judge, L. Wang, Y. Y. L. Ho and Y. Wang, *Macromol. Res.*, 2018, **26**, 1074–1084.

31 D. Rota Martir and E. Zysman-Colman, *Chem. Commun.*, 2019, **55**, 139–158.

32 X. Jing, C. He, L. Zhao and C. Duan, *Acc. Chem. Res.*, 2019, **52**, 100–109.

33 M. L. Saha, X. Yan and P. J. Stang, *Acc. Chem. Res.*, 2016, **49**, 2527–2539.

34 P. Wei, X. Yan, T. R. Cook, X. Ji, P. J. Stang and F. Huang, *ACS Macro Lett.*, 2016, **5**, 671–675.

35 S. Kobayashi, M. L. Saha and P. J. Stang, *J. Organomet. Chem.*, 2017, **847**, 294–297.

36 G.-F. Huo, X. Shi, Q. Tu, Y.-X. Hu, G.-Y. Wu, G.-Q. Yin, X. Li, L. Xu, H.-M. Ding and H.-B. Yang, *J. Am. Chem. Soc.*, 2019, **141**, 16014–16023.

37 L. Xu, X. Shen, Z. Zhou, T. He, J. Zhang, H. Qiu, M. L. Saha, S. Yin and P. J. Stang, *J. Am. Chem. Soc.*, 2018, **140**, 16920–16924.

38 M. Zhang, S. Li, X. Yan, Z. Zhou, M. L. Saha, Y.-C. Wang and P. J. Stang, *Proc. Natl. Acad. Sci. U. S. A.*, 2016, **113**, 11100–11105.

39 Y. Sun, F. Ding, Z. Chen, R. Zhang, C. Li, Y. Xu, Y. Zhang, R. Ni, X. Li, G. Yang, Y. Sun and P. J. Stang, *Proc. Natl. Acad. Sci. U. S. A.*, 2019, **116**, 16729–16735.

40 Y. Sun, F. Ding, Z. Zhou, C. Li, M. Pu, Y. Xu, Y. Zhan, X. Lu, H. Li, G. Yang, Y. Sun and P. J. Stang, *Proc. Natl. Acad. Sci. U. S. A.*, 2019, **116**, 1968–1973.

41 M. Zhang, S. Yin, J. Zhang, Z. Zhou, M. L. Saha, C. Lu and P. J. Stang, *Proc. Natl. Acad. Sci. U. S. A.*, 2017, **114**, 3044–3049.

42 V. Gupta and S. K. Mandal, *Dalton Trans.*, 2018, **47**, 9742–9754.

43 A. Garci, K. J. Castor, J. Fakhoury, J.-L. Do, J. Di Trani, P. Chidchob, R. S. Stein, A. K. Mittermaier, T. Friscic and H. Sleiman, *J. Am. Chem. Soc.*, 2017, **139**, 16913–16922.

44 X. Chang, Z. Zhou, C. Shang, G. Wang, Z. Wang, Y. Qi, Z.-Y. Li, H. Wang, L. Cao, X. Li, Y. Fang and P. J. Stang, *J. Am. Chem. Soc.*, 2019, **141**, 1757–1765.

45 J. Plutnar, C. Givelet, C. Lemouchi, J. Jaklová Dytrtová, I. Císařová, S. J. Teat and J. Michl, *Organometallics*, 2019, **38**, 4633–4644.

46 Z. Zhou, D.-G. Chen, M. L. Saha, H. Wang, X. Li, P.-T. Chou and P. J. Stang, *J. Am. Chem. Soc.*, 2019, **141**, 5535–5543.

47 W. Wang, Z. Zhou, J. Zhou, B. Shi, B. Song, X. Li, F. Huang and P. J. Stang, *Inorg. Chem.*, 2019, **58**, 7141–7145.

48 J. Y. Ryu, J. M. Lee, N. Nguyen Van, K. M. Lee, S. Lee, M. H. Lee, P. J. Stang and J. Lee, *Inorg. Chem.*, 2018, **57**, 11696–11703.

49 M. Zhang, H. Xu, M. Wang, M. L. Saha, Z. Zhou, X. Yan, H. Wang, X. Li, F. Huang, N. She and P. J. Stang, *Inorg. Chem.*, 2017, **56**, 12498–12504.

50 Y. Yang, J.-S. Chen, J.-Y. Liu, G.-J. Zhao, L. Liu, K.-L. Han, T. R. Cook and P. J. Stang, *J. Phys. Chem. Lett.*, 2015, **6**, 1942–1947.

51 N. Liu, T. Lin, M. Wu, H.-K. Luo, S.-L. Huang and T. S. A. Hor, *J. Am. Chem. Soc.*, 2019, **141**, 9448–9452.

52 G. Yu, Y. Ye, Z. Tong, J. Yang, Z. Li, B. Hua, L. Shao and S. Li, *Macromol. Rapid Commun.*, 2016, **37**, 1540–1547.

53 Y. Sun, F. Zhang, S. Jiang, Z. Wang, R. Ni, H. Wang, W. Zhou, X. Li and P. J. Stang, *J. Am. Chem. Soc.*, 2018, **140**, 17297–17307.

54 Y. Sun, Y. Yao, H. Wang, W. Fu, C. Chen, M. L. Saha, M. Zhang, S. Datta, Z. Zhou, H. Yu, X. Li and P. J. Stang, *J. Am. Chem. Soc.*, 2018, **140**, 12819–12828.

55 C. Lu, M. Zhang, D. Tang, X. Yan, Z. Zhang, Z. Zhou, B. Song, H. Wang, X. Li, S. Yin, H. Sepehrpour and P. J. Stang, *J. Am. Chem. Soc.*, 2018, **140**, 7674–7680.

56 X. Yan, T. R. Cook, P. Wang, F. Huang and P. J. Stang, *Nat. Chem.*, 2015, **7**, 342–348.

57 M. Zhang, M. L. Saha, M. Wang, Z. Zhou, B. Song, C. Lu, X. Yan, X. Li, F. Huang, S. Yin and P. J. Stang, *J. Am. Chem. Soc.*, 2017, **139**, 5067–5074.

58 G. Yu, B. Zhu, L. Shao, J. Zhou, M. L. Saha, B. Shi, Z. Zhang, T. Hong, S. Li, X. Chen and P. J. Stang, *Proc. Natl. Acad. Sci. U. S. A.*, 2019, **116**, 6618–6623.

59 Y. Ye, T. R. Cook, S.-P. Wang, J. Wu, S. Li and P. J. Stang, *J. Am. Chem. Soc.*, 2015, **137**, 11896–11899.

60 L. Cao, P. Wang, X. Miao, H. Duan, H. Wang, Y. Dong, R. Ma, B. Zhang, B. Wu, X. Li and P. J. Stang, *Inorg. Chem.*, 2019, **58**, 6268–6275.

61 L. Cao, P. Wang, X. Miao, Y. Dong, H. Wang, H. Duan, Y. Yu, X. Li and P. J. Stang, *J. Am. Chem. Soc.*, 2018, **140**, 7005–7011.

62 B. Jiang, J. Zhang, W. Zheng, L.-J. Chen, G.-Q. Yin, Y.-X. Wang, B. Sun, X. Li and H.-B. Yang, *Chem. – Eur. J.*, 2016, **22**, 14664–14671.

63 V. S. P. K. Neti, M. L. Saha, X. Yan, Z. Zhou and P. J. Stang, *Organometallics*, 2015, **34**, 4813–4815.

64 J.-H. Tang, Y. Li, Q. Wu, Z. Wang, S. Hou, K. Tang, Y. Sun, H. Wang, H. Wang, C. Lu, X. Wang, X. Li, D. Wang, J. Yao, C. J. Lambert, N. Tao, Y.-W. Zhong and P. J. Stang, *Nat. Commun.*, 2019, **10**, 4599.

65 X. Yan, H. Wang, C. E. Hauke, T. R. Cook, M. Wang, M. L. Saha, Z. Zhou, M. Zhang, X. Li, F. Huang and P. J. Stang, *J. Am. Chem. Soc.*, 2015, **137**, 15276–15286.

66 Q. Zhang, D. Tang, J. Zhang, R. Ni, L. Xu, T. He, X. Lin, X. Li, H. Qiu, S. Yin and P. J. Stang, *J. Am. Chem. Soc.*, 2019, **141**, 17909–17917.

67 Y. Sun, S. Li, Z. Zhou, M. L. Saha, S. Datta, M. Zhang, X. Yan, D. Tian, H. Wang, L. Wang, X. Li, M. Liu, H. Li and P. J. Stang, *J. Am. Chem. Soc.*, 2018, **140**, 3257–3263.

68 Y. Ye, S.-P. Wang, B. Zhu, T. R. Cook, J. Wu, S. Li and P. J. Stang, *Org. Lett.*, 2015, **17**, 2804–2807.

69 J. Zhou, Y. Zhang, G. Yu, M. R. Crawley, C. R. P. Fulong, A. E. Friedman, S. Sengupta, J. Sun, Q. Li, F. Huang and T. R. Cook, *J. Am. Chem. Soc.*, 2018, **140**, 7730–7736.

70 Z. Zhou, X. Yan, M. L. Saha, M. Zhang, M. Wang, X. Li and P. J. Stang, *J. Am. Chem. Soc.*, 2016, **138**, 13131–13134.

71 Z. Yue, H. Wang, Y. Li, Y. Qin, L. Xu, D. J. Bowers, M. Gangoda, X. Li, H.-B. Yang and Y.-R. Zheng, *Chem. Commun.*, 2018, **54**, 731–734.

72 W. Zheng, L.-J. Chen, G. Yang, B. Sun, X. Wang, B. Jiang, G.-Q. Yin, L. Zhang, X. Li, M. Liu, G. Chen and H.-B. Yang, *J. Am. Chem. Soc.*, 2016, **138**, 4927–4937.

This journal is © The Royal Society of Chemistry 2020

Chem. Soc. Rev., 2020, **49**, 3889–3919 | **3917**

73 L.-J. Chen, S. Chen, Y. Qin, L. Xu, G.-Q. Yin, J.-L. Zhu, F.-F. Zhu, W. Zheng, X. Li and H.-B. Yang, *J. Am. Chem. Soc.*, 2018, **140**, 5049–5052.

74 G.-Y. Wu, X.-Q. Wang, L.-J. Chen, Y.-X. Hu, G.-Q. Yin, L. Xu, B. Jiang and H.-B. Yang, *Inorg. Chem.*, 2018, **57**, 15414–15420.

75 A. Baba, T. Kojima and S. Hiraoka, *Chem. – Eur. J.*, 2018, **24**, 838–847.

76 W. Zheng, W. Wang, S.-T. Jiang, G. Yang, Z. Li, X.-Q. Wang, G.-Q. Yin, Y. Zhang, H. Tan, X. Li, H. Ding, G. Chen and H.-B. Yang, *J. Am. Chem. Soc.*, 2019, **141**, 583–591.

77 J.-H. Tang, Y. Sun, Z.-L. Gong, Z.-Y. Li, Z. Zhou, H. Wang, X. Li, M. L. Saha, Y.-W. Zhong and P. J. Stang, *J. Am. Chem. Soc.*, 2018, **140**, 7723–7729.

78 K. Acharyya, S. Bhattacharyya, H. Sepehrpour, S. Chakraborty, S. Lu, B. Shi, X. Li, P. S. Mukherjee and P. J. Stang, *J. Am. Chem. Soc.*, 2019, **141**, 14565–14569.

79 Z. Zhou, J. Liu, J. Huang, T. W. Rees, Y. Wang, H. Wang, X. Li, H. Chao and P. J. Stang, *Proc. Natl. Acad. Sci. U. S. A.*, 2019, **116**, 20296–20302.

80 S. Datta, M. L. Saha, N. Lahiri, G. Yu, J. Louie and P. J. Stang, *Org. Lett.*, 2018, **20**, 7020–7023.

81 D. Zhang, D. Li, X. Li and W. Jin, *Dyes Pigm.*, 2018, **152**, 43–48.

82 A. Chowdhury, P. Howlader and P. S. Mukherjee, *Chem. – Eur. J.*, 2016, **22**, 7468–7478.

83 Y. Qin, L.-J. Chen, F. Dong, S.-T. Jiang, G.-Q. Yin, X. Li, Y. Tian and H.-B. Yang, *J. Am. Chem. Soc.*, 2019, **141**, 8943–8950.

84 Z. Zhou, X. Yan, T. R. Cook, M. L. Saha and P. J. Stang, *J. Am. Chem. Soc.*, 2016, **138**, 806–809.

85 S. Datta, S. K. Misra, M. L. Saha, N. Lahiri, J. Louie, D. Pan and P. J. Stang, *Proc. Natl. Acad. Sci. U. S. A.*, 2018, **115**, 8087–8092.

86 Y.-X. Wang, Q.-F. Zhou, S.-T. Jiang, Y. Zhang, G.-Q. Yin, B. Jiang, X. Li, H. Tan and H.-B. Yang, *Macromol. Rapid Commun.*, 2018, **39**, 1800454.

87 X. Yan, M. Wang, T. R. Cook, M. Zhang, M. L. Saha, Z. Zhou, X. Li, F. Huang and P. J. Stang, *J. Am. Chem. Soc.*, 2016, **138**, 4580–4588.

88 Y. Tian, X. Yan, M. L. Saha, Z. Niu and P. J. Stang, *J. Am. Chem. Soc.*, 2016, **138**, 12033–12036.

89 E. Martinou, K. Seintis, N. Karakostas, A. Bletsou, N. S. Thomaidis, M. Fakis and G. Pistolis, *J. Phys. Chem. C*, 2017, **121**, 5341–5355.

90 B. Shi, Z. Zhou, R. T. Vanderlinden, J.-H. Tang, G. Yu, K. Acharyya, H. Sepehrpour and P. J. Stang, *J. Am. Chem. Soc.*, 2019, **141**, 11837–11841.

91 B. Shi, Y. Liu, H. Zhu, R. T. Vanderlinden, L. Shangguan, R. Ni, K. Acharyya, J.-H. Tang, Z. Zhou, X. Li, F. Huang and P. J. Stang, *J. Am. Chem. Soc.*, 2019, **141**, 6494–6498.

92 B. Jiang, J. Zhang, J.-Q. Ma, W. Zheng, L.-J. Chen, B. Sun, C. Li, B.-W. Hu, H. Tan, X. Li and H.-B. Yang, *J. Am. Chem. Soc.*, 2016, **138**, 738–741.

93 B. Song, Z. Zhang, K. Wang, C.-H. Hsu, O. Bolarinwa, J. Wang, Y. Li, G.-Q. Yin, E. Rivera, H.-B. Yang, C. Liu, B. Xu and X. Li, *Angew. Chem., Int. Ed.*, 2017, **56**, 5258–5262.

94 Z. He, M. Li, W. Que and P. J. Stang, *Dalton Trans.*, 2017, **46**, 3120–3124.

95 C. C. Givelet, P. I. Dron, J. Wen, T. F. Magnera, M. Zamadar, K. Cepe, H. Fujiwara, Y. Shi, M. R. Tuchband, N. Clark, R. Zboril and J. Michl, *J. Am. Chem. Soc.*, 2016, **138**, 6676–6687.

96 Z. Li, X. Yan, F. Huang, H. Sepehrpour and P. J. Stang, *Org. Lett.*, 2017, **19**, 5728–5731.

97 A. Jana, S. Bhowmick, S. Kaur, H. K. Kashyap and N. Das, *Dalton Trans.*, 2017, **46**, 1986–1995.

98 S. Bhowmick, A. Jana, K. Singh, P. Gupta, A. Gangrade, B. B. Mandal and N. Das, *Inorg. Chem.*, 2018, **57**, 3615–3625.

99 R.-L. Zhang, Y. Yang, S.-Q. Yang and K.-L. Han, *Phys. Chem. Chem. Phys.*, 2018, **20**, 2205–2210.

100 I. A. Bhat, A. Devaraj, P. Howlader, K.-W. Chi and P. S. Mukherjee, *Chem. Commun.*, 2018, **54**, 4814–4817.

101 H. Li, T.-Z. Xie, Z. Liang, D. Dahal, Y. Shen, X. Sun, Y. Yang, Y. Pang and T. Liu, *Chem. Commun.*, 2019, **55**, 330–333.

102 M. Zhang, M. L. Saha and P. J. Stang, *Struct. Chem.*, 2017, **28**, 453–459.

103 G. Yu, T. R. Cook, Y. Li, X. Yan, D. Wu, L. Shao, J. Shen, G. Tang, F. Huang, X. Chen and P. J. Stang, *Proc. Natl. Acad. Sci. U. S. A.*, 2016, **113**, 13720–13725.

104 G. Yu, S. Yu, M. L. Saha, J. Zhou, T. R. Cook, B. C. Yung, J. Chen, Z. Mao, F. Zhang, Z. Zhou, Y. Liu, L. Shao, S. Wang, C. Gao, F. Huang, P. J. Stang and X. Chen, *Nat. Commun.*, 2018, **9**, 4335.

105 Z. Zhou, C. E. Hauke, B. Song, X. Li, P. J. Stang and T. R. Cook, *J. Am. Chem. Soc.*, 2019, **141**, 3717–3722.

106 Z. He, Z. Hou, Y. Xing, X. Liu, X. Yin, M. Que, J. Shao, W. Que and P. J. Stang, *Sci. Rep.*, 2016, **6**, 29476.

107 J.-H. Tang, R. Ni, Y.-Q. He, R. T. Vanderlinden, Y. Li, B. Shi, Z.-Y. Li, H. Wang, X. Li, Y. Sun, Y.-W. Zhong and P. J. Stang, *Inorg. Chem.*, 2019, **58**, 13376–13381.

108 O. Domarco, D. Loetsch, J. Schreiber, C. Dinhof, S. Van Schoonhoven, M. D. Garcia, C. Peinador, B. K. Keppler, W. Berger and A. Terenzi, *Dalton Trans.*, 2017, **46**, 329–332.

109 H. Wang, Z. Qiu, H. Liu, A. M. D. S. Jayawardhana, Z. Yue, H. Daghlas, D. J. Bowers, B. Datta and Y.-R. Zheng, *Front. Chem.*, 2019, **7**, 39.

110 A. Ahmedova, R. Mihaylova, D. Momekova, P. Shestakova, S. Stoykova, J. Zaharieva, M. Yamashina, G. Momekov, M. Akita and M. Yoshizawa, *Dalton Trans.*, 2016, **45**, 13214–13221.

111 M. Yamashina, M. Akita, T. Hasegawa, S. Hayashi and M. Yoshizawa, *Sci. Adv.*, 2017, **3**, e1701126.

112 M. Yamashina, S. Kusaba, M. Akita, T. Kikuchi and M. Yoshizawa, *Nat. Commun.*, 2018, **9**, 4227.

113 E. Kalenius, M. Groessl and K. Rissanen, *Nat. Rev. Chem.*, 2019, **3**, 4–14.

114 C. Mallis, M. Lal Saha and P. Stang, *J. Am. Soc. Mass Spectrom*, 2019, **30**, 1654–1662.

115 R.-L. Zhang, Y. Yang, S.-Q. Yang, V. S. P. K. Neti, H. Sepehrpour, P. J. Stang and K.-L. Han, *J. Phys. Chem. C*, 2017, **121**, 14975–14980.

116 F. J. Rizzuto, L. K. S. von Krbek and J. R. Nitschke, *Nat. Rev. Chem.*, 2019, **3**, 204–222.

117 Y. Ye, S.-P. Wang, B. Zhu, T. R. Cook, J. Wu, S. Li and P. J. Stang, *Org. Lett.*, 2015, **17**, 2804–2807.

118 N. Hosono and S. Kitagawa, *Acc. Chem. Res.*, 2018, **51**, 2437–2446.

119 Y. Sun, C. Chen and P. J. Stang, *Acc. Chem. Res.*, 2019, **52**, 802–817.

120 B. Li, T. He, Y. Fan, X. Yuan, H. Qiu and S. Yin, *Chem. Commun.*, 2019, **55**, 8036–8059.

121 L. Zhao, X. Jing, X. Li, X. Guo, L. Zeng, C. He and C. Duan, *Coord. Chem. Rev.*, 2019, **378**, 151–187.

122 S. Gao, X. Yan, G. Xie, M. Zhu, X. Ju, P. J. Stang, Y. Tian and Z. Niu, *Proc. Natl. Acad. Sci. U. S. A.*, 2019, **116**, 23437–23443.

123 C. M. Hong, R. G. Bergman, K. N. Raymond and F. D. Toste, *Acc. Chem. Res.*, 2018, **51**, 2447–2455.

124 L. R. Holloway, P. M. Bogie, Y. Lyon, C. Ngai, T. F. Miller, R. R. Julian and R. J. Hooley, *J. Am. Chem. Soc.*, 2018, **140**, 8078–8081.

125 A. N. Oldacre, A. E. Friedman and T. R. Cook, *J. Am. Chem. Soc.*, 2017, **139**, 1424–1427.

126 A. N. Oldacre, M. R. Crawley, A. E. Friedman and T. R. Cook, *Chem. – Eur. J.*, 2018, **24**, 10984–10987.

127 J. Jiao, Z. Li, Z. Qiao, X. Li, Y. Liu, J. Dong, J. Jiang and Y. Cui, *Nat. Commun.*, 2018, **9**, 4423.

128 S. S. Nurttila, W. Brenner, J. Mosquera, K. M. van Vliet, J. R. Nitschke and J. N. H. Reek, *Chem. – Eur. J.*, 2019, **25**, 609–620.

This journal is © The Royal Society of Chemistry 2020

Chem. Soc. Rev., 2020, **49**, 3889–3919 | **3919**